

# Transcriptomic entropy quantifies cardiomyocyte maturation at single cell level

Suraj Kannan<sup>a,b,c</sup>, Michael Farid<sup>b</sup>, Brian L. Lin<sup>a</sup>, Matthew Miyamoto<sup>a</sup>, and Chulan Kwon<sup>a,c,\*</sup>

<sup>a</sup>Division of Cardiology, Department of Medicine, Johns Hopkins School of Medicine; <sup>b</sup>Department of Biomedical Engineering, Johns Hopkins School of Medicine; <sup>c</sup>Institute for Cell Engineering, Johns Hopkins School of Medicine

This manuscript was compiled on April 2, 2020

**While pluripotent stem cell-derived cardiomyocytes (PSC-CMs) offer tremendous potential for a range of clinical applications, their use has been constrained by the failure to mature these cells to a fully adult-like phenotype. Extensive efforts are currently underway with the goal to mature PSC-CMs. However, comprehensive metrics to benchmark the maturation status and trajectory of PSC-CMs have not been established. Here, we developed a novel approach to quantify CM maturation through single cell transcriptomic entropy. We found that transcriptomic entropy is robust across datasets regardless of differences in isolation protocols, library preparation methods, and other potential batch effects. We analyzed over 40 single cell RNA-sequencing (scRNA-seq) datasets and over 45,000 CMs to establish a cross-study, cross-species reference of CM maturation based on transcriptomic entropy. We subsequently computed the maturation status of PSC-CMs by direct comparison to *in vivo* development. Our study presents a robust, interpretable, and easy-to-use metric for quantifying CM maturation.**

cardiomyocyte | transcriptomic | single cell

The development of robust protocols for generation of cardiomyocytes (CMs) from pluripotent stem cells (PSCs) has represented a huge advance in cardiovascular medicine over the past two decades. Adult CMs are notably non-proliferative and difficult to obtain from patients, and thus deriving PSC-CMs is currently the most viable method for generating large quantities of human CMs (1). PSC-CMs have numerous promised applications towards cardiac health, including regenerative medicine, drug efficacy and toxicity screening, and *in vitro* disease modeling (2–6). However, clinical application of PSC-CMs has been limited thus far due to the failure of these cells to mature to a fully adult-like phenotype *ex vivo*. During the course of normal development, CMs undergo a lengthy maturation process characterized by adaptive changes to structure, function, gene expression, and metabolism (7). By contrast, PSC-CMs resemble embryonic CMs, even following extended culture (8). Thus, solving the so-called “maturation problem” in PSC-CMs is a major target for cardiovascular research.

To date, numerous *ex vivo* approaches have been proposed to improve PSC-CM maturation. These approaches have included cytokine, growth factor, and hormone cocktails, co-culture with other cells, induction of physical stimuli (e.g. mechanical stretch, electrical stimulation), and construction of biomaterial-based three dimensional tissues, typically with the goal of recapitulating important aspects the native cardiac milieu (8–11). Benchmarking the efficacy of these interventions has been challenging, however, due to a lack of established standards for quantifying CM maturation (8). In particular, direct comparisons between PSC-CMs and mature adult CMs are limited both due to the difficulty of culturing adult CMs

long term and the challenge in performing many conventional CM functional assays (e.g. sarcomeric shortening) with PSC-CMs (12, 13). Correspondingly, most interventions to improve PSC-CM maturation are compared against an *in vitro* control or at best one discrete (usually neonatal) *in vivo* timepoint, rather than across the continuous spectrum of *in vivo* CM maturation. Several groups have aimed to use -omics data to compare PSC-CMs to *in vivo* CMs (14–16). However, these approaches have been limited to bulk samples, which precludes their use for highly heterogeneous PSC-CM populations.

scRNA-seq has emerged as a powerful tool for measuring the transcriptomes of large numbers of single cells. The development of new isolation protocols has facilitated the use of scRNA-seq for cardiac tissues (17, 18), making it an intriguing candidate for new metrics of PSC-CM maturation. Unfortunately, differences in isolation protocols, library preparation methods, and sequencing machines, among other factors, can imbue scRNA-seq data with batch effects that are difficult to deconvolve (19, 20). In turn, this makes it difficult to directly compare expression of individual genes across datasets. While batch correction algorithms have been developed (21), they are primarily designed for correcting or integrating datasets with multiple well-defined cell types with significantly different gene expression patterns rather than one continuously evolving cell type. Thus, an optimal scRNA-seq-based metric of CM maturation must be robust to batch effects and facilitate direct comparison of maturation status independent of the method used to generate the data.

Here, we develop an approach based on quantifying gene *distributions* to assess CM maturation. Our approach is based on the generally-observed phenomenon that less

## Significance Statement

There is significant interest in generating mature cardiomyocytes from pluripotent stem cells. However, there are currently few effective metrics to quantify the maturation status of a single cardiomyocyte. We developed a new metric for measuring cardiomyocyte maturation using single cell RNA-sequencing data. This metric, called entropy score, uses the gene distribution to estimate maturation at the single cell level. Entropy score enables comparing pluripotent stem cell-derived cardiomyocytes directly against endogenously-isolated cardiomyocytes. Thus, entropy score can better assist in development of approaches to improve the maturation of pluripotent stem cell-derived cardiomyocytes.

The authors have no competing interests to declare.

\*To whom correspondence should be addressed. E-mail: [ckwon13jhmi.edu](mailto:ckwon13jhmi.edu)

differentiated cells are typically more promiscuous in their expression of signaling pathways, leading to a diverse gene expression profile. However, as they differentiate, they prune unnecessary signaling pathways and hone in on a relatively narrow gene expression profile (22). This observation underlies our understanding of cellular differentiation (23), and has been leveraged in several previous approaches to study differentiation of stem cells to progenitors and subsequently to committed lineages (24–28). We apply this principle to study the maturation of committed CMs by developing a metric based on a modification of the Shannon entropy of gene expression in scRNA-seq data. We find that our transcriptomic entropy-based metric not only adequately stages single CMs, but that transcriptomic entropy scores are consistent across datasets regardless of potentially confounding batch effects. Using datasets from the literature, we perform a meta-analysis of CM maturation based on transcriptomic entropy. We subsequently demonstrate the use of our approach to infer the maturation status of PSC-CMs, with the goal of establishing transcriptomic entropy as a viable metric of CM maturation.

## Results

**Shannon entropy of single cell gene expression decreases over CM maturation.** Following terminal differentiation, CMs undergo a lengthy maturation process characterized by gradual and unidirectional changes in gene expression (15). Based on previous findings, we proposed a model for transcriptional

maturation of CMs analogous to cellular differentiation (Figure 1A). In this model, nascent cardiomyocytes express a broad gene expression profile. However, as they mature, they slowly reduce expression of immature gene pathways (e.g. cell cycle) while upregulating genes required for mature function (e.g. sarcomere, calcium handling, oxidative phosphorylation). These gradual changes in gene distribution can be quantified by established diversity metrics such as the well-known Shannon entropy. In our model, immature myocytes will present with high transcriptomic entropy, which subsequently decreases in a continuous manner over the course of maturation.

To test the validity of this model, we generated an scRNA-seq library of ~1,000 CMs from 12 timepoints over the course of maturation. Sequencing of postnatal CMs, which are large and fragile, has been previously limited (29). Recently, however, we developed a method to isolate healthy adult CMs to generate high quality scRNA-seq libraries using large-particle fluorescence-activated cell sorting (LP-FACS) (18). We used this approach to isolate CMs from *Myh6-Cre; mTmG* (aMHC-cre x mTmG) mice, in which cells expressing cardiac-specific myosin heavy chain are readily separated by GFP expression (Figure 1B). Our maturation reference particularly sampled cells within the first three weeks postnatally, as this period may be critically relevant to the maturation process but is underrepresented in existing CM scRNA-seq datasets.

We next computed the Shannon entropy  $S$  on the unique molecular identifier (UMI) counts of our maturation reference

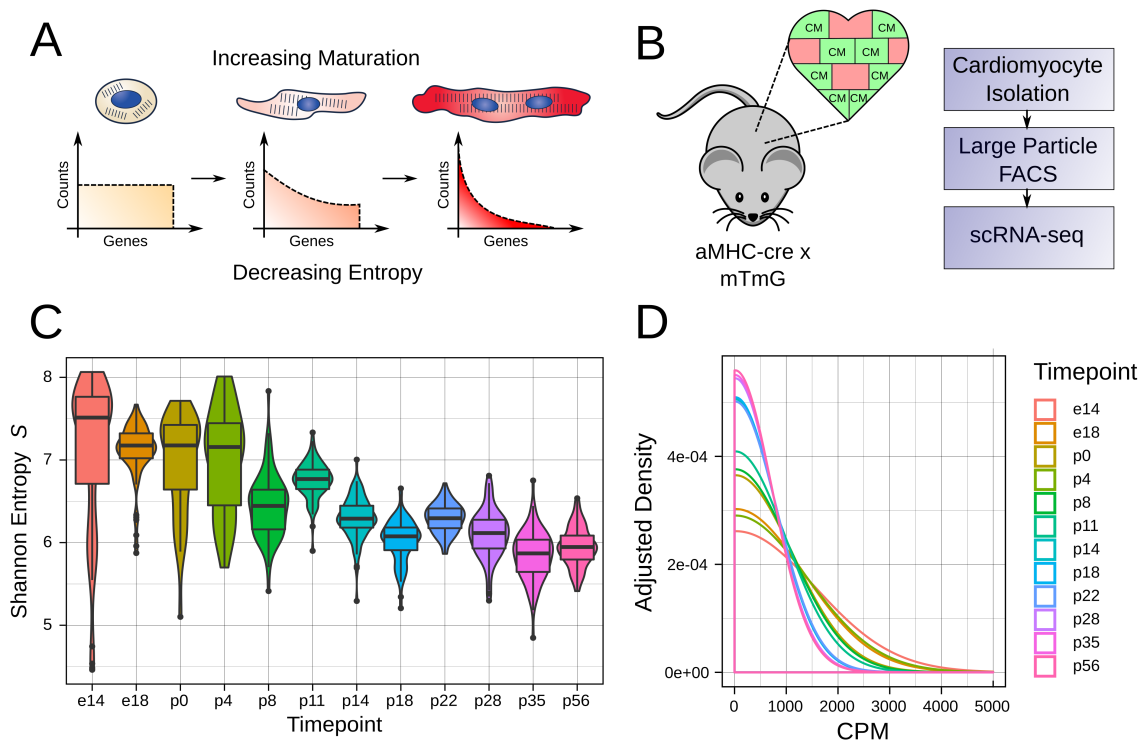


**Fig. 1. Shannon entropy of the single cell transcriptome shows a characteristic decrease over CM maturation.** **A.** Our model for changes in gene distribution over CM maturation. As CMs undergo the maturation process, they transition from a broad gene distribution (characterised by high entropy) to a more narrow distribution (characterised by low entropy). **B.** Mouse model used to generate perinatal maturation reference scRNA-seq library. In the aMHC-cre x mTmG mouse, CMs are labeled by GFP. **C.** Shannon Entropy  $S$  computed for each timepoint in the maturation reference dataset. **D.** Smoothed density estimates for genes expressed at 0-5000 counts per million (CPM) for each timepoint in the maturation reference dataset.

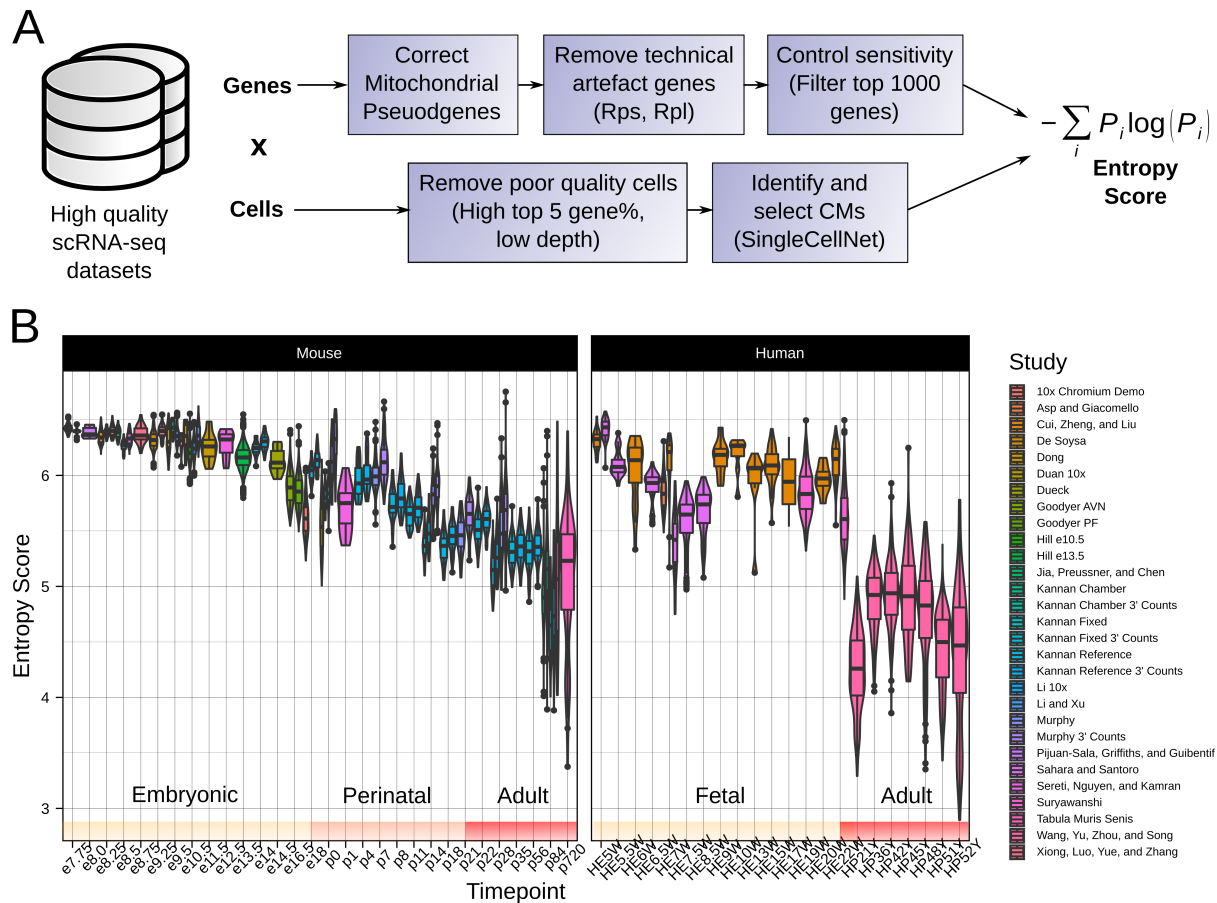


**Fig. 2. Entropy score enables cross-study and cross-species comparison of CM maturation status.** **A.** Workflow for computing entropy score from high quality scRNA-seq datasets. Details are further discussed in **Supplementary Notes 1-5**. **B.** Entropy score for mouse and human *in vivo* CMs taken from publicly available datasets.

(**Figure 1C**). Entropy gradually decreased from e14 to p56, with a notable shift from p4 to p8, thereby supporting our hypothesized entropy model. We additionally plotted the averaged gene distributions for each timepoint (**Figure 1D**). As expected, earlier timepoints showed a more broad distribution compared to later timepoints. These results supported the use of Shannon entropy to quantify CM maturation status from scRNA-seq data.

**Entropy score enables cross-study inference of maturation status.** Given the correspondence between Shannon entropy and CM maturation status, we next sought to determine whether we could extend our transcriptomic entropy model to many CM scRNA-seq datasets generated across multiple labs. However, several technical challenges prevented accurate cross-study comparison of Shannon entropy computed on raw, unfiltered datasets. Therefore, we developed a workflow for addressing major technical confounding variables to enabling cross-study comparisons (**Figure 2A**). The rationale for each step is discussed in **Figures S1-S5** and **Supplementary Notes 1-5**. Briefly, our workflow first corrected reads incorrectly mapped to mitochondrial pseudogenes, an artefact of certain genomic read mapping/counting pipelines (**Figure S1, Supplementary Note 1**). We removed ribosomal protein coding genes, as their expression level may be biased by certain sequencing protocols (**Figure S2, Supplementary**

**Note 2**). We then selected the top 1000 highest expressed genes in each cell. This step is particularly important as it controls for sensitivity differences both between cells and across datasets. Poor quality cells were filtered using two metrics - the percentage of counts in the 5 highest expressed genes (a potential read-out of cell lysis) and unusually low depth (**Figure S3, Supplementary Note 3**). Further issues regarding dataset quality are addressed in **Figure S4** and **Supplementary Note 4**. We lastly identified cells with CM gene expression signatures using SingleCellNet (30) (**Figure S5, Supplementary Note 5**). The output of our workflow is the computed Shannon entropy on the filtered datasets, which we refer to as *entropy score* through the remainder of the manuscript. Entropy score is robust to multiple commonly used read-mapping/counting pipelines (**Figure S1**), sequencing protocols (**Figure S6**), and sequencing depths, with the exception of very low-depth Drop-seq datasets (**Figure S7, Supplementary Note 6**).

To test the utility of entropy score in quantifying CM maturation, we identified publicly available scRNA-seq datasets containing CMs isolated *in vivo* (**Supplementary Table 1**). Our meta-analysis included 32 mouse datasets and 5 human datasets, and after filtration contained 35,378 CMs spanning numerous timepoints across the range of development. Additionally, the collected datasets represented significant diversity in terms of isolation methods, sequencing protocols,

mapping/counting pipelines, and datatypes (including reads from full-length scRNAseq protocols, 3' counts from UMI protocols prior to UMI collapsing, and UMIs). Entropy score gradually decreased over developmental time, as hypothesized by our model (**Figure 2B**, **Figure S8**). Notably, despite the marked heterogeneity of dataset characteristics, entropy score was consistent at similar timepoints across multiple datasets. This was true even for datasets whose batch effects were difficult to resolve through integration methods (**Figure S9**). In particular, entropy score showed remarkable concordance between datasets featuring different datatypes. For example, using four UMI-based datasets generated by our group, we found that the ratio of entropy score computed prior to versus after UMI collapsing was 1.02 (**Figure S10**).

In the mouse *in vivo* datasets, entropic changes occurred in three broad phases (**Figure 2B**). In the embryonic phase ( $\sim e7.75$ - $e16.5$ ), entropy score decreased at a relatively slow rate. Upon initiation of the perinatal phase at  $e16.5$ , entropy score decreased more rapidly before converging onto a relatively mature adult-like phase at p21. These changes correspond well to previous literature about the dynamics of CM maturation, in particular regarding the perinatal maturation window (7).

We were additionally curious about the efficacy of entropy score to capture the maturation status of human CMs. We found that there was good concordance in entropy score between stage-matched mouse and human tissues (**Figure 2B**). In particular, fetal tissues (ranging from embryonic week 5 to embryonic week 22) corresponded to  $\sim e13.5$ - $e14.5$  in mice, while adult human CMs were comparable to adult mouse CMs. We did observe that one dataset (Sahara et al.) showed a notably lower entropy score at embryonic weeks 7-8, though

we suspect this may have to do with dataset quality issues (**Supplementary Note 4**). Taken as a whole, however, these results support the use of entropy score as a cross-study, cross-species metric of CM maturation.

**Entropy score recapitulates gene expression trends in CM maturation.** We next tested whether entropy score computationally ordered single CMs based on their progression along the maturation process, akin to so-called trajectory inference or pseudotime analysis methods. We selected three well-known trajectory inference methods - Monocle 2, Slingshot, and SCORPIUS - based on their performance in recent benchmarking studies, particularly with reconstructing unidirectional topologies (31). We then performed trajectory inference with our maturation reference dataset and compared the resultant pseudotimes with entropy score. Additionally, we identified genes differentially expressed over pseudotime/entropy score for each method respectively. Entropy score correlated only moderately with pseudotimes for the three methods (**Figure 3A**, **Figure S11**). However, there was notable overlap in identified differentially expressed genes (**Figure 3B**). In particular,  $\sim 93.6\%$  of genes identified as differentially expressed over entropy score were also identified by at least one other method, and  $\sim 81.5\%$  were identified as differentially expressed by all methods. Moreover, when treated as a pseudotime metric, entropy score accurately recapitulated known CM maturation gene expression trends (**Figure 3C**). We further tested entropy score as a pseudotime metric in datasets composed of only one biological timepoint but a range of entropy scores. Intriguingly, gene expression trends across entropy score in these one-timepoint datasets

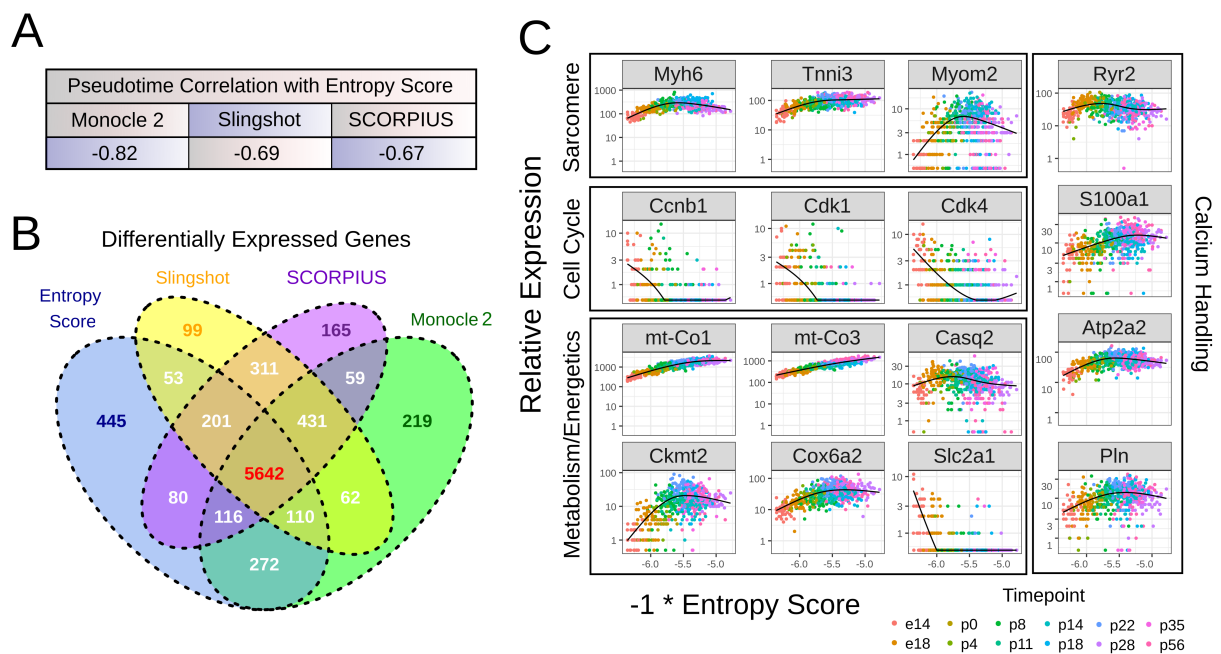


**Fig. 3. Entropy score functions as a pseudotime score for CM maturation.** **A.** Pearson correlation between entropy score and calculated pseudotimes for our maturation reference dataset for three trajectory inference methods: Monocle 2, Slingshot, and SCORPIUS. **B.** Venn diagram showing overlap in identified differentially expressed genes between entropy score and trajectory inference methods. Differentially expressed genes were identified by fitting generalized additive models to gene trends over the corresponding pseudotime in Monocle 2, and selecting genes with adjusted p-value  $< 0.05$ . **C.** Gene expression trends over entropy score for genes involved in CM maturation, including sarcomeric, cell cycle, metabolism, and calcium handling genes.

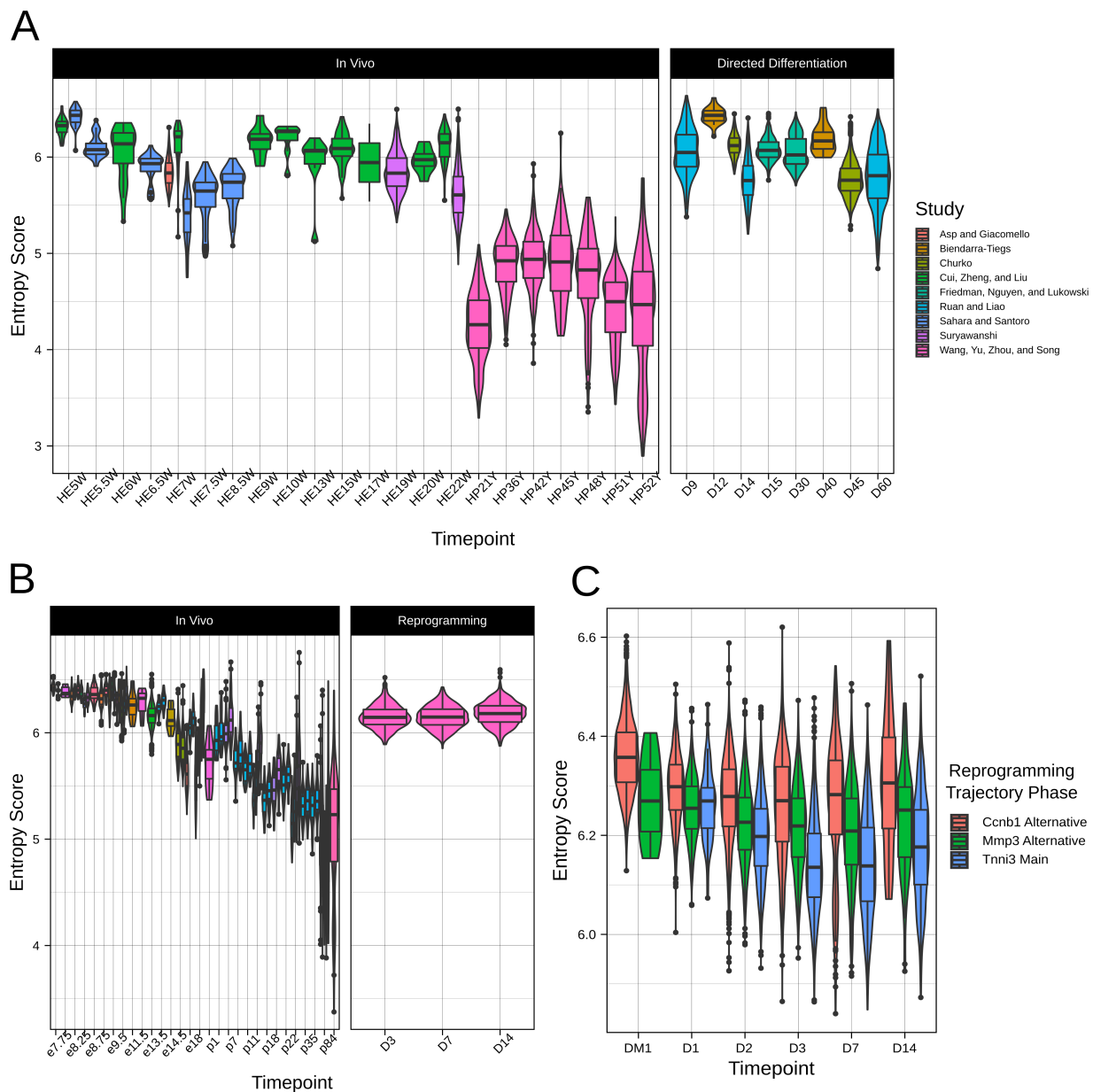


**Fig. 4. Entropy score quantifies maturation status of PSC-CMs and iCMs. A.** Comparison in entropy score between human *in vivo* CMs and human PSC-CMs. Left side of figure reproduced from **Figure 2B**. **B.** Comparison in entropy between mouse *in vivo* CMs and mouse iCMs. Left side of figure reproduced from **Figure 2B**. **C.** Entropy score for three reprogramming pathways - a canonical *Tnni2+* iCM pathway and two alternative pathways (*Ccnb1+* and *Mmp3+*).

largely matched the trends observed in our maturation reference dataset (**Figure S12**). These results suggest that entropy score can effectively reconstruct the CM maturation trajectory as it occurs heterogeneously at the single cell level, and can accurately quantify single CM maturation status regardless of the biological timepoint of the sample.

#### Human PSC-CMs do not mature beyond embryonic stage.

Having validated entropy score as a metric of CM maturation *in vivo*, we next tested the entropy score of PSC-CMs from publicly available datasets (**Supplementary Table 2**). We identified 5 datasets of directed differentiation of human induced PSCs to CMs, and analyzed 6,397 cells between D(day)9 and D60 of differentiation post-filtering. Though

there was some variation from study to study (perhaps due to line-to-line differences or variations in differentiation protocol), there was a modest decrease in entropy score over the course of differentiation (**Figure 4A**). However, no study generated CMs with an entropy score lower than human fetal tissues, confirming the immature nature of PSC-CMs. Moreover, there was limited change in entropy score between D45 and D60 PSC-CMs, suggestive of maturation arrest. Interestingly, the entropy score of these later timepoint PSC-CMs corresponded to the initiation of the perinatal phase of mouse CM maturation *in vivo*. This observation may point to dysregulation of the endogenous perinatal maturation program during *in vitro* directed differentiation as a cause of poor PSC-CM maturation status, and merits further investigation.

**Reprogrammed CMs present with embryonic-like maturation status.** In addition to directed differentiation of PSCs, another approach that has been explored to generate CMs *ex vivo* is direct reprogramming of fibroblasts to CM-like cells (iCMs) by transcription factor, microRNA, and cytokine cocktails (32). We used entropy score to analyze a dataset of reprogramming of mouse neonatal fibroblasts to iCMs by overexpression of Gata4, Mef2c, and Tbx5. Focusing only on cells with CM-like signature, we found that entropy score showed limited change between D3 and D14 of reprogramming (**Figure 4B**). iCMs remained at a mid-embryonic stage of maturation, comparable to e13.5-e14.5 in mouse *in vivo* CMs. Moreover, compared to PSC-CMs at the same timepoint of differentiation, iCMs displayed higher entropy. This result matches earlier findings that direct reprogramming less effectively recapitulates native gene regulatory networks compared to directed differentiation (33).

We further explored change in entropy score across multiple reprogramming pathways. The authors of the dataset identified a branching reprogramming trajectory (34). Reprogrammed cells entered either a canonical iCM route (e.g. Tnni3+) or two alternative pathways - one characterised by activation of Mmp3 and another marked by cell cycle progression (e.g. Ccnb1+). Using the authors' annotations, we classified all cells in the dataset (including those without a CM signature) into one of these three pathways and assessed the entropy score for cells in each pathway (**Figure 4C**). At D1 of reprogramming, cells in all three pathways show similar entropy score. However, from D1 to D3, cells in the canonical iCM pathway show more notable decrease in entropy score, and indeed remain at a lower entropy score than cells in other pathways. Thus, while iCMs still present with a notably immature status compared to *in vivo*, they display some improvement in maturation status compared to cells arrested in alternative reprogramming pathways.

## Discussion

Here, we present the use of transcriptomic entropy score for quantifying CM maturation at the single cell level. Our approach builds on the well-known Shannon entropy to generate a metric of CM maturation from scRNA-seq data that is robust to a range of sequencing protocols and potential batch effects. In particular, entropy score enables direct benchmarking of *in vitro* PSC-CM maturation against their *in vivo* counterparts. This is particularly important because endogenous CM development is the gold standard for instructing PSC-CM maturation. Correspondingly, we believe that perturbations to improve PSC-CM maturation must be compared against this gold standard rather than an *in vitro* control. Our newly developed entropy score enables comparison of PSC-CMs against the full trajectory of endogenous CM maturation. Entropy score can thus be used to better assess PSC-CM maturation methodologies, and guide development of tissues that better recapitulate the adult CM phenotype. It should be noted, however, that we do not see entropy score as the end-all for CM maturation quantification. In addition to potential discrepancies between transcript and protein level expression (35), the mature CM phenotype encompasses numerous functional parameters that may be only partially captured at the transcriptomic level. We envision entropy score as complementing existing functional

assays to advance a more complete assessment of single CM maturation status.

Through meta-analysis of over 40 scRNA-seq datasets of CMs, we were able to gain some insights into the dynamics of CM maturation. In particular, we were interested to note the existence of a perinatal phase of maturation *in vivo*, initiating at approximately e16.5-e18.5, during which CM entropy score rapidly decreased. Entropy score continued to decrease until approximately ~3-4 weeks postnatally. We previously hypothesized the existence of a critical perinatal window for CM maturation, and postulated that disruption of this window *in vitro* leads to maturation arrest (7). The significant decrease in entropy observed in our study supports the perinatal window hypothesis. Moreover, late-stage PSC-CMs remained arrested at an entropy score similar to those of e16.5 CMs *in vivo*. To date, mechanistic understanding of PSC-CM maturation arrest has been limited, but may involve progressive disruption of cardiac gene regulatory networks (15). Our results suggest that increased focus should be placed on trying to understand regulators of perinatal maturation *in vivo*, and determining discrepancies in activity of these regulators *in vitro*.

In this study, we found that entropy score could be applied to scRNA-seq datasets generated from a wide range of protocols. Excluding the quality control steps, entropy score is computed from information in one cell at a time, independent of other cells or datasets. Nevertheless, entropy score shows strong concordance with CM maturation status in a comparable manner across dataset. This is particular novel as, thus far, direct comparisons across studies has been limited by confounding batch effects. Moreover, current batch correction algorithms may be poorly suited to integration of datasets along a continuous trajectory. For example, anecdotally, we found that several popular batch correction algorithms failed to correctly coalesce CMs from similar timepoints even when handling only two datasets. Moreover, scaling batch correction algorithms to many datasets may be complex and computationally intensive. By contrast, entropy score has limited computational demands and can scale easily to allow for comparison of many datasets.

We were particularly intrigued to note the comparability of entropy scores across datasets with entirely different datatypes (e.g. reads, UMIs). For example, it is well known that PCR amplification in scRNA-seq protocols can lead to biases (36), which was one of the motivations for the development of UMIs. However, entropy scores were comparable for UMI datasets prior to and after collapsing UMIs. Likewise, datasets generated from full-length protocols did not display notable biases in entropy score. This observation may have been incidental to the datasets we studied - for example, high quality datasets may have presented with sufficiently low amplification bias to enable comparison. It is possible that entropy score is less robust to more extreme cases of amplification bias. We do not believe our finding precludes the use of best practices for scRNA-seq protocols, including the use of UMIs for many experimental designs. Nevertheless, we were encouraged that entropy score could be used to facilitate cross-comparison between otherwise incompatible datatypes.

One technical limitation of entropy score was its poor performance with Drop-seq datasets. We consistently found that Drop-seq datasets presented with higher entropy than

data generated at similar timepoints through other protocols. This may be a consequence of depth; the Drop-seq datasets that we tested were the lowest depth studies tested and below our identified optimal depth threshold. However, given the increasing prevalence of other high-quality droplet-based protocols (in particular, 10x Chromium), we believe this is not a major limiting factor to the use of entropy score. We additionally did not test single nuclear RNA-seq datasets, both due to concerns of depth and because we expected that the gene distribution would be inherently different from whole cell studies (37). Nevertheless, the emergence of methods for isolation of whole adult CMs in mouse and human (17, 18, 38) may reduce the future need for nuclear RNA-seq.

At the single cell level, CM maturation proceeds heterogeneously along a unidirectional trajectory (39). We were therefore curious to know the extent to which entropy score could capture single cell positioning along this trajectory, in effect functioning as a pseudotime metric. Entropy score only modestly correlated with other established pseudotime methods, though all methods recovered similar differentially expressed genes. These discrepancies may be due to transcriptomic noise in single cell data. However, it should be emphasized that entropy score works in a fundamentally different manner than many trajectory inference methods. Most trajectory inference methods utilize some type of dimensionality reduction step prior to curve fitting. By contrast, outside of the subselection of highly expressed genes, entropy score uses no dimensionality reduction step. Moreover, entropy score makes no assumptions about relationships between cells – all relevant information is calculated independently for each cell. Despite being agnostic to cell-cell relationships, entropy score accurately captures CM maturation expression trends. Commonly used dimensionality reduction methods have been shown to distort local neighbourhoods and affect trajectory reconstruction (40), and thus entropy score may more optimally capture single CM dynamics in maturation.

Entropy score has several important antecedents that must be acknowledged. Our work is similar to StemID (28), which uses Shannon entropy to assign progenitor state within a trajectory. We extend this usage with several gene filtering steps to better facilitate cross-study comparison. Shannon entropy is also utilized in SLICE (26), which computes entropy based on functional annotations of genes, and SCENT (24), which computes entropy within a protein-protein interaction network. Both approaches are powerful for constructing trajectories for differentiating cells. However, unlike differentiation, CM maturation is characterized by continuous rather than step-wise or switch-like changes. For this purpose, an entropy score built directly on gene expression levels is both simpler to compute and more appropriate. Lastly, our work is similar conceptually to CytoTRACE (27), which leverages gene diversity to order cells by differentiation status. Directly comparing number of genes expressed by each cell is confounded by cross-study differences in depth and sensitivity, however. CytoTRACE addresses this by using a smoothing step within dataset. However, this limits its use for datasets with few cells or representing fewer maturation states. By contrast, outside of quality filtering, entropy score performs computations on each cell independently, extending its utility to more datasets.

Our focus in this manuscript was towards the quantification of PSC-CM maturation status. In theory, however, our work is easily extensible to other biological contexts. In particular, questions of maturation status have been raised with regards to other PSC-derived tissues, such as hepatocytes (41) and neurons (42). We expect that application of entropy score to these systems will improve assessment of PSC-derived tissue quality and enable development of improved tissues for clinical use.

## Materials and Methods

All methods, including wet lab and computational methods, can be found in the Supplementary Information. Raw data for the maturation reference can be found on GEO at GSE147807. Code to generate figures in this manuscript as well as the counts tables for the datasets analyzed in this manuscript can be found on Github at <https://github.com/skannan4/cm-entropy-score>.

**ACKNOWLEDGMENTS.** We thank Dr. Deborah Andrew for allowing us to use her group's COPAS LP-FACS instrument. Sequencing experiments were done through the Johns Hopkins Transcriptomics and Deep Sequencing Core, with the help of Dr. Haiping Hao, Linda Orzolek, Dr. Jasmeet Sethi, and Kelly Laughlin. We additionally thank Dr. Marc Halushka, Dr. Patrick Cahlan, Stephanie Yang, and Yuqi Tan for helpful comments in preparing this manuscript.

1. I Batalov, AW Feinberg, Differentiation of cardiomyocytes from human pluripotent stem cells using monolayer culture. *Biomark. Insights* **10**, 71–76 (2015).
2. R Passier, C Denning, C Mummery, Cardiomyocytes from Human Embryonic Stem Cells. *Stem Cells Handb. Exp. Pharmacol.* **1**, 101–122 (2006).
3. BC du Pré, PA Doevendans, LW van Laake, Stem cells for cardiac repair: an introduction. *J. geriatric cardiology : JGC* **10**, 186–97 (2013).
4. W Wang, X Chen, S Houser, C Zeng, Potential of cardiac stem/progenitor cells and induced pluripotent stem cells for cardiac repair in ischaemic heart disease. *Clin. Sci.* **125**, 319–327 (2013).
5. IY Chen, E Matsa, JC Wu, Induced pluripotent stem cells: At the heart of cardiovascular precision medicine. *Nat. Rev. Cardiol.* **13**, 333–349 (2016).
6. AA Youssef, et al., The Promise and Challenge of Induced Pluripotent Stem Cells for Cardiovascular Applications. *JACC: Basic to Transl. Sci.* **1**, 510–523 (2016).
7. S Kannan, C Kwon, Regulation of cardiomyocyte maturation during critical perinatal window. *J. Physiol.* **0**, 1–16 (2019).
8. NT Feric, M Radisic, Maturing human pluripotent stem cell-derived cardiomyocytes in human engineered cardiac tissues. *Adv. Drug Deliv. Rev.* **96**, 110–134 (2016).
9. R Zhu, et al., Physical developmental cues for the maturation of human pluripotent stem cell-derived cardiomyocytes. *Stem cell research & therapy* **5**, 117 (2014).
10. AH Nguyen, et al., Cardiac tissue engineering : state-of-the-art methods and outlook. *J. Biol. Eng.* **13**, 1–21 (2019).
11. GJ Scuderi, J Butcher, Naturally Engineered Maturation of Cardiomyocytes. *Front. Cell Dev. Biol.* **5**, 1–28 (2017).
12. GS Cho, et al., Neonatal Transplantation Confers Maturation of PSC-Derived Cardiomyocytes Conducive to Modeling Cardiomyopathy. *Cell Reports* **18**, 571–582 (2017).
13. AJS Ribeiro, et al., Contractility of single cardiomyocytes differentiated from pluripotent stem cells depends on physiological shape and substrate stiffness. *Proc. Natl. Acad. Sci.* **112**, 12705–12710 (2015).
14. W Cai, et al., An Unbiased Proteomics Method to Assess the Maturation of Human Pluripotent Stem Cell-Derived Cardiomyocytes. *Circ. Res.* **125**, 936–953 (2019).
15. H Uosaki, et al., Transcriptional Landscape of Cardiomyocyte Maturation. *Cell Reports* **13**, 1705–1716 (2015).
16. CW van den Berg, et al., Transcriptome of human foetal heart compared with cardiomyocytes from pluripotent stem cells. *Development* **142**, 3231–3238 (2015).
17. M Yekelchik, S Guenther, J Preussner, T Braun, Mono - and multi - nucleated ventricular cardiomyocytes constitute a transcriptionally homogenous cell population. *Basic Res. Cardiol.* **114**, 1–13 (2019).
18. S Kannan, et al., Large particle fluorescence-activated cell sorting enables high-quality single-cell RNA sequencing and functional analysis of adult cardiomyocytes. *Circ. Res.* (2019).
19. O Stegle, SA Teichmann, JC Marioni, Computational and analytical challenges in single-cell transcriptomics. *Nat. Rev. Genet.* **16** (2015).
20. Py Tung, et al., Batch effects and the effective design of single-cell gene expression studies. *Sci. Reports* **7**, 1–15 (2017).
21. HTN Tran, et al., A benchmark of batch-effect correction methods for single-cell RNA sequencing data. *Genome Biol.* **21**, 1–32 (2020).
22. AE Teschendorff, P Sollich, R Kuehn, Signalling entropy : A novel network-theoretical framework for systems analysis and interpretation of functional omic data. *Methods* **67**, 282–293 (2014).

23. BD MacArthur, IR Lemischka, Statistical Mechanics of Pluripotency. *Cell* **154**, 484–489 (2013).
24. AE Teschendorff, T Enver, Single-cell entropy for accurate estimation of differentiation potency from a cell's transcriptome. *Nat. Commun.* **8**, 1–15 (2017).
25. W Chen, AE Teschendorff, Estimating Differentiation Potency of Single Cells Using Single-Cell Entropy (SCENT). *Comput. Methods for Single-Cell Data Analysis* **1935**, 125–139 (2019).
26. M Guo, EL Bao, M Wagner, JA Whitsett, Y Xu, SLICE : determining cell differentiation and lineage based on single cell entropy. *Nucleic Acids Res.* **45**, 1–14 (2017).
27. GS Gulati, et al., Single-cell transcriptional diversity is a hallmark of developmental potential. *Science* **367**, 405–411 (2020).
28. D Grun, et al., De Novo Prediction of Stem Cell Identity using Resource De Novo Prediction of Stem Cell Identity using Single-Cell Transcriptome Data. *Cell Stem Cell* **19**, 266–277 (2016).
29. M Ackers-johnson, W Lek, W Tan, RSy Foo, Following hearts, one cell at a time : recent applications of single-cell RNA sequencing to the understanding of heart disease. *Nat. Commun.*, 8–11 (2018).
30. Y Tan, P Cahan, SingleCellNet: a computational tool to classify single cell RNA-Seq data across platforms and across species. *bioRxiv* (2018).
31. W Saelens, R Cannoodt, H Todorov, Y Saeys, A comparison of single-cell trajectory inference methods. *Nat. Biotechnol.* **37** (2019).
32. H Tani, T Sadahiro, M Ieda, Direct Cardiac Reprogramming : A Novel Approach for Heart Regeneration. *Int. J. Mol. Sci.* **19**, 1–13 (2018).
33. P Cahan, H Li, SA Morris, E Lummertz, GQ Daley, CellNet : Network Biology Applied to Stem Cell Engineering. *Cell* **158**, 903–915 (2014).
34. NR Stone, et al., Context-Specific Transcription Factor Functions Regulate Epigenomic and Transcriptional Dynamics during Cardiac Reprogramming. *Cell Stem Cell* **25**, 87–102.e9 (2019).
35. WR Blevins, et al., Extensive post-transcriptional buffering of gene expression in the response to severe oxidative stress in baker's yeast. *Sci. reports* **9**, 1–11 (2019).
36. S Islam, et al., Quantitative single-cell RNA-seq with unique molecular identifiers. *Nat. Methods* **11** (2014).
37. A Selewa, et al., Systematic Comparison of High- throughput Single-Cell and Single- Nucleus Transcriptomes during Cardiomyocyte Differentiation. *Sci. Reports* **10**, 1–13 (2020).
38. L Wang, et al., Single-cell reconstruction of the adult human heart during heart failure and recovery reveals the cellular landscape underlying cardiac function. *Nat. Cell Biol.* **22** (2020).
39. S Murphy, et al., PGC1 / PPAR Drive Cardiomyocyte Maturation through Regulation of Yap1 and SF3B2. *bioRxiv* (2020).
40. SM Cooley, T Hamilton, EJ Deeds, JCJ Ray, A novel metric reveals previously unrecognized distortion in dimensionality reduction of scRNA-Seq data. *bioRxiv*, 1–36 (2019).
41. JL Corbett, SA Duncan, iPSC-Derived Hepatocytes as a Platform for Disease Modeling and Drug Discovery. *Front. Medicine* **6**, 1–12 (2019).
42. Yy Wu, FI Chiu, Cs Yeh, Hc Kuo, Opportunities and challenges for the use of induced pluripotent stem cells in modelling neurodegenerative disease. *Open Biol.* **9** (2019).



THE PREPRINT SERVER FOR BIOLOGY

## Supplementary Information for

### Transcriptomic entropy quantifies cardiomyocyte maturation at single cell level

Suraj Kannan, Michael Farid, Brian L. Lin, Matthew Miyamoto, Chulan Kwon

Corresponding Author: Chulan Kwon

E-mail: [ckwon13@jhmi.edu](mailto:ckwon13@jhmi.edu)

#### This PDF file includes:

- Supplementary Notes 1 to 6
- Figs. S1 to S12
- Supplementary Methods
- Appendix
- SI References

## Supporting Information Text

The purpose of these supplementary notes is to discuss critical features that went into the design of our entropy score metric. While the general principles of entropy score are straightforward, we utilized several gene and cell filtration steps to optimize cross-study comparison. We outline our decisions here and provide rationale to support our approach.

Shannon entropy has had long-standing applications in developmental biology as well as transcriptional analysis (1, 2). A standard form for Shannon entropy  $S$  is:

$$S = - \sum_i P_i \log(P_i)$$

where  $P_i$  represents individual probabilities for events of interest. Here, we define  $P_i$  as the probability of selecting a given gene  $i$  in a cell. From scRNA-seq data, this can be computed by simply dividing the number of counts for gene  $i$  by all of the gene counts in a given cell. For our entropy score, we similarly use Shannon entropy, except after subsetting the top 1000 highest expressed genes to enable sensitivity control.

**Supplementary Note 1: Handling multiple mapping/counting pipelines.** There are a large number of pipelines for generating count matrices from raw RNA-seq data. In particular, there are numerous approaches for mapping raw RNA-seq reads to either genome or transcriptome, and subsequently counting mapped reads. While there have been benchmarking studies to compare pipelines (3), there is still no consensus on optimal approaches for generating count matrices. One of the goals of our study was to ensure that entropy score could be broadly and easily usable by many users with a range of data generation methods. Where possible we aimed to use count matrices generated by the original manuscript authors regardless of pipeline used, though in some cases we remapped or recounted as necessary (see **Appendix** for more details).

One problem that was regularly observed was the incorrect mapping of mitochondrial reads to pseudogenes. In mice, fragments of the mitochondrial genome are present as pseudogenes in the nuclear genome (termed nuclear mitochondrial insertion sequences (4)). These fragments often show identical or near-identical sequences to mitochondrial genes, and thus reads are often multi-mapped between canonical mitochondrial genes and pseudogenes. Multi-mapping reads are handled differently by different pipelines. However, in pipelines counting multi-mapping reads, we often found high numbers of mitochondrial pseudogenes - for example, Gm29216, Gm28437, Gm28661, Gm13340, and others. This issue was particularly problematic for CMs, as they naturally express high amounts of mitochondrial genes (5). Accurate quantification of these genes was thus necessary for cross-study accuracy of entropy score.

As our goal was to enable entropy score to be widely usable across many protocols, we included an approximate pseudogene correction in our pipeline. We made the assumption that CMs do not express mitochondrial pseudogenes to any appreciable extent, and thus all identified pseudogenes could be converted to the corresponding mitochondrial gene. We identified cross-mappings between pseudogenes and canonical genes, and subsequently removed all pseudogene counts and added them to the corresponding canonical mitochondrial genes. It must be noted that this approach is an approximation. For example, for UMI datasets, if UMI collapsing is done after gene identification, this method may overestimate mitochondrial counts. Additionally, we only focused on correcting mitochondrial pseudogene mismappings, as these most affected our data. However, it is possible that other genes are also mismapped.

To test the efficacy of our pseudogene correction, we tested the entropy score and well as mitochondrial gene percentages before and after correction for several mapping/counting methods (**Figure S1**). As a genomic method, we used the zUMIs pipeline (6), which uses STAR for mapping followed by FeatureCounts for counting. In this method, multimapping counts are effectively randomly allocated between mitochondrial reads and pseudogenes. As a transcriptomic method, we utilized kallisto|bustools (7). We used kallisto|bustools with two indices – a full index containing all mouse cDNAs from ENSEMBL (kb.full), and an index containing only protein coding, lincRNAs, and antisense RNAs analogous to the Cell Ranger index (kb.cellranger). Lastly, we also used Cell Ranger, a part of the 10x Genomics pipeline. Cell Ranger first maps reads to the genome, and subsequently takes mapped reads and remaps against a transcriptome. However, as stated above, the Cell Ranger index does not contain pseudogenes, and thus does not feature mitochondrial read mismapping.

We tested zUMIs, kb.full, and kb.cellranger for our maturation reference data pre- and post-correction (**Figure S1A, S1B**), as well as the 10x Chromium dataset with zUMIs, kb.full, kb.cellranger, and Cell Ranger (**Figure S1C, S1D**). As expected, prior to correction, zUMIs and kb.full produced datasets with lower mitochondrial read percentage and therefore higher entropy. However, post-correction, these datasets showed entropy and mitochondrial read percentages that were nearly identical to kb.cellranger and Cell Ranger. Thus, our recommendation to users is to either use Cell Ranger or kallisto|bustools with a Cell Ranger index. In the case that this is not possible, however, datasets that include multi-mapping reads will be sufficiently corrected for use in our entropy score.

**Supplementary Note 2: Gene filtering.** By default, entropy score only uses genes with gene biotype “protein coding,” “antisense,” or “lincRNAs,” so as to focus on the key players of the transcriptome. We additionally considered ribosomal protein-coding genes (e.g. starting with “Rps” or “Rpl” in mouse and “RPS” or “RPL” in human). These genes are often discarded or ignored during analysis. We plotted the expression of these genes in mouse *in vivo* datasets over time (**Figure S2A**) and found no clear maturation-related effect in terms of expression of these genes. However, there were significant protocol-related biases in terms of expression of these genes (**Figure S2B**). In particular, 10x Chromium and STRT-seq datasets appeared to have

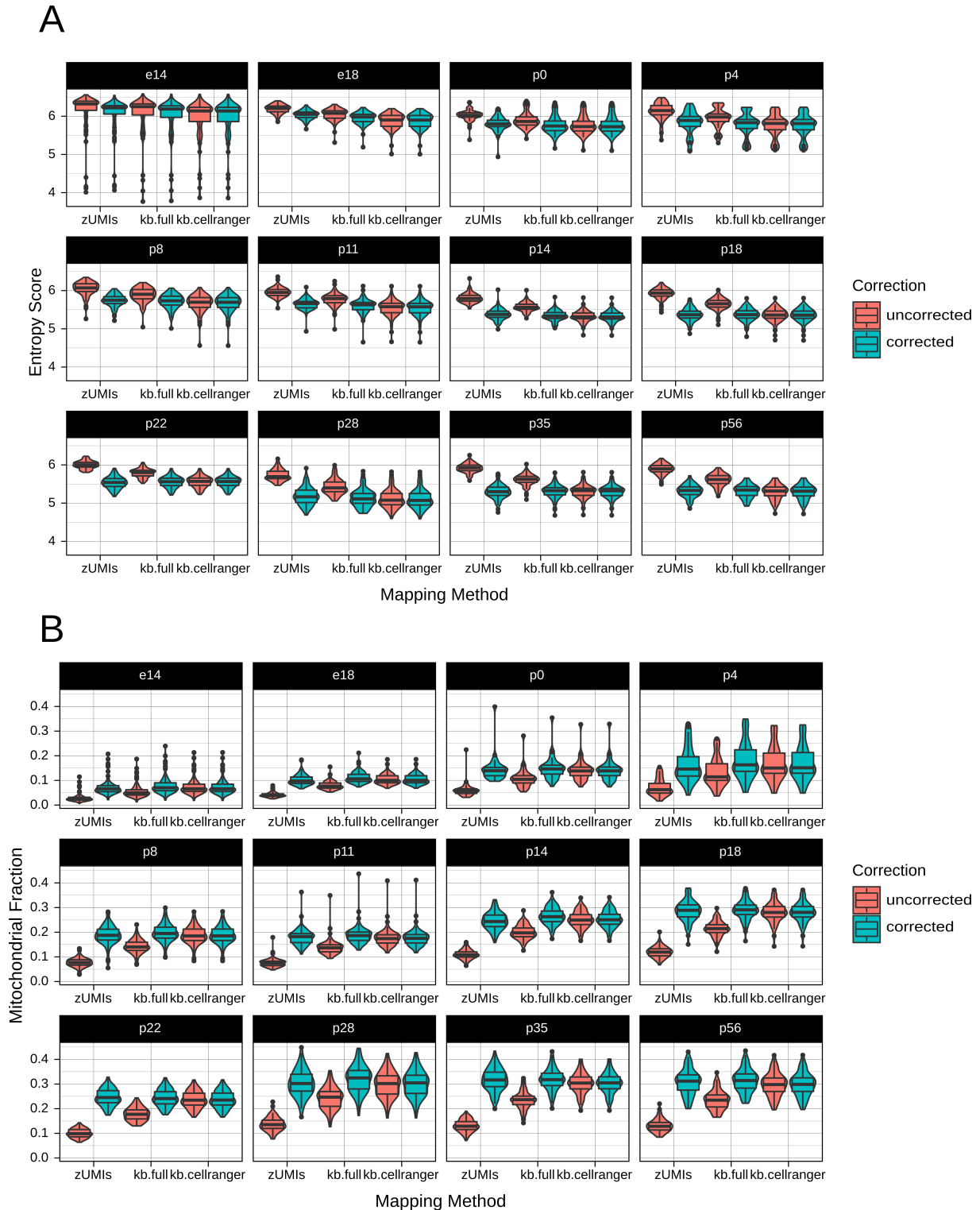


**Fig. S1. Correction of mitochondrial pseudogenes enables consistent entropy score measurements across mapping/counting pipelines. A.** Entropy scores for the maturation reference dataset mapped by zUMIs, kallisto|bustools with the full reference, and kallisto|bustools with the CellRanger reference. Pre- and post-correction scores are shown. **B.** As in A, showing mitochondrial proportions. *Figure continues on next page.*

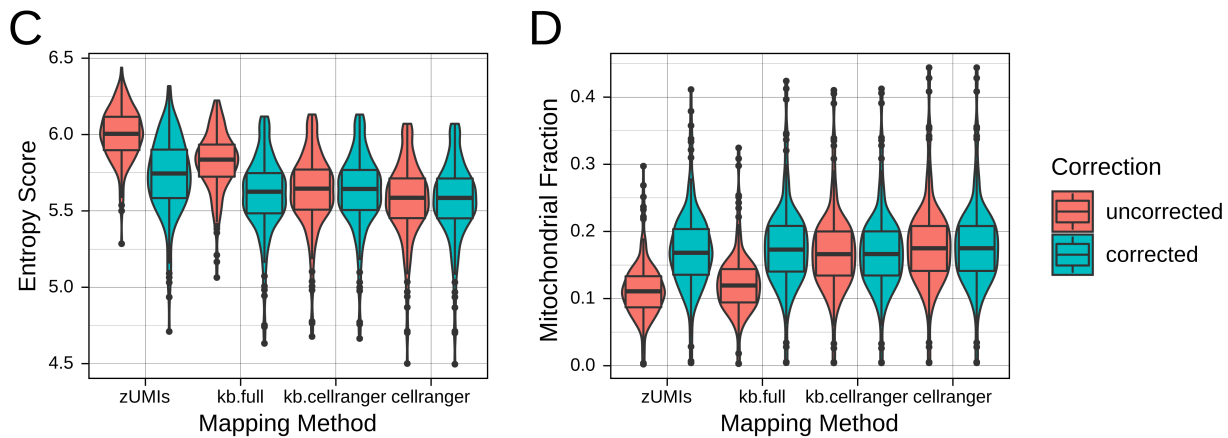


**Fig. S1.** (Continued from previous page.) **C.** Entropy scores for the 10x Chromium heart dataset mapped by zUMIs, kallisto|bustools with the full reference, kallisto|bustools with the CellRanger reference, and CellRanger. **D.** As in C, showing mitochondrial proportions.

systematically higher percentages of ribosomal protein-coding genes than other protocols. This observation anecdotally matches observations made by others and likely indicates a protocol bias, though we are unsure about the reason this occurs. There was no compelling reason for believing that the expression level of these genes related to CM maturation status; however, their expression skewed gene distributions in certain datasets. Therefore, we removed all ribosomal protein-coding genes prior to computation of entropy score.

**Supplementary Note 3: Quality control of poor-quality cells.** Quality control is an essential step in all scRNA-seq protocols (8–10). Protocols will inevitably generate cells that have been lysed or damaged in some way, making them unsuitable for downstream analysis. A range of metrics have been used to assess poor quality cells. However, there are no set standards for indication of poor quality. There are technical and biological reasons for this limitation. For example, a metric such as mitochondrial read percentage (often used to mark cell lysis), will be dependent not only on tissue type (11) (particularly with regards to CMs), but also on biological timepoint. Likewise, a metric such as numbers of counts/genes expressed is inherently dataset specific - 5000 counts may be the median for a high quality cell in a low-depth study, but may indicate a lysed cell in a high-depth study. Thus, quality control is often done in a study-to-study manner.

As our study involves a meta-analysis of many independently generated datasets, we aimed to establish a standardized approach for quality control. This had the dual benefits of ensuring at least a minimal level of comparability while limiting the need to determine individual thresholds for each dataset. We focused on two primary metrics of quality control - cell depth and percentage of reads going to the top 5 highest expressed genes in each cell. We selected these metrics because we observed that they most affected quantification of entropy score. As an example, we plotted the Churko et al. data (Figure S3A, S3B). Both low depth and high percentage of top 5 reads (usually, though not always, mitochondrial reads) led to artificially low entropy score, requiring filtering. We particularly observed large tails of artificially low entropy cells in datasets with many cells, such as 10x Chromium-generated datasets.

We then defined normalized metrics based on both measurements by dividing the respective measurement by the median of that measure in that study and in that timepoint. Thus, while comparable cross-study, the metrics could be considered with respect to potential biological and technical variation. We then set the threshold for the normalized depth metric as  $> -0.5$  (Figure S3C) and the normalized top5 percent metric as  $< 1.3$  (Figure S3D).

There are some caveats to our approach. Firstly, we selected very conservative thresholds. We initially tested several different thresholds and found that being more conservative could do a better job in eliminating poor quality cells without dramatically affecting higher quality cells; however, these thresholds are still essentially subjective and may require further optimization. Secondly, while we aimed to standardize our quality control process, it must be observed that our input data itself is inconsistent - many of the datasets already had some level of quality control before being input into our pipeline. Given the biological concordance between entropy score and maturation, we believe that any variations in quality control based on input data were minimal. Nevertheless, this is an area that will continue to require further discussion and decision-making from the scRNA-seq community.

**Supplementary Note 4: Identifying poor quality datasets.** One additional caveat to our approach outlined in Supplementary Note 3 is the assumption that a dataset is broadly high quality but contains some low quality cells. This assumption is violated when the entire dataset itself is poor quality. For example, adult CMs are highly difficult to isolate at the single cell level by a number of classical methods, such as conventional FACS, single cell picking, or microfluidic devices such as the Fluidigm C1. We have previously shown that these methods can yield poor quality scRNA-seq, where the percentage of identified mitochondrial reads is far in excess of that in a bulk control (5). However, because such datasets are globally affected, our outlined quality control approach will incorrectly allow cells to pass.

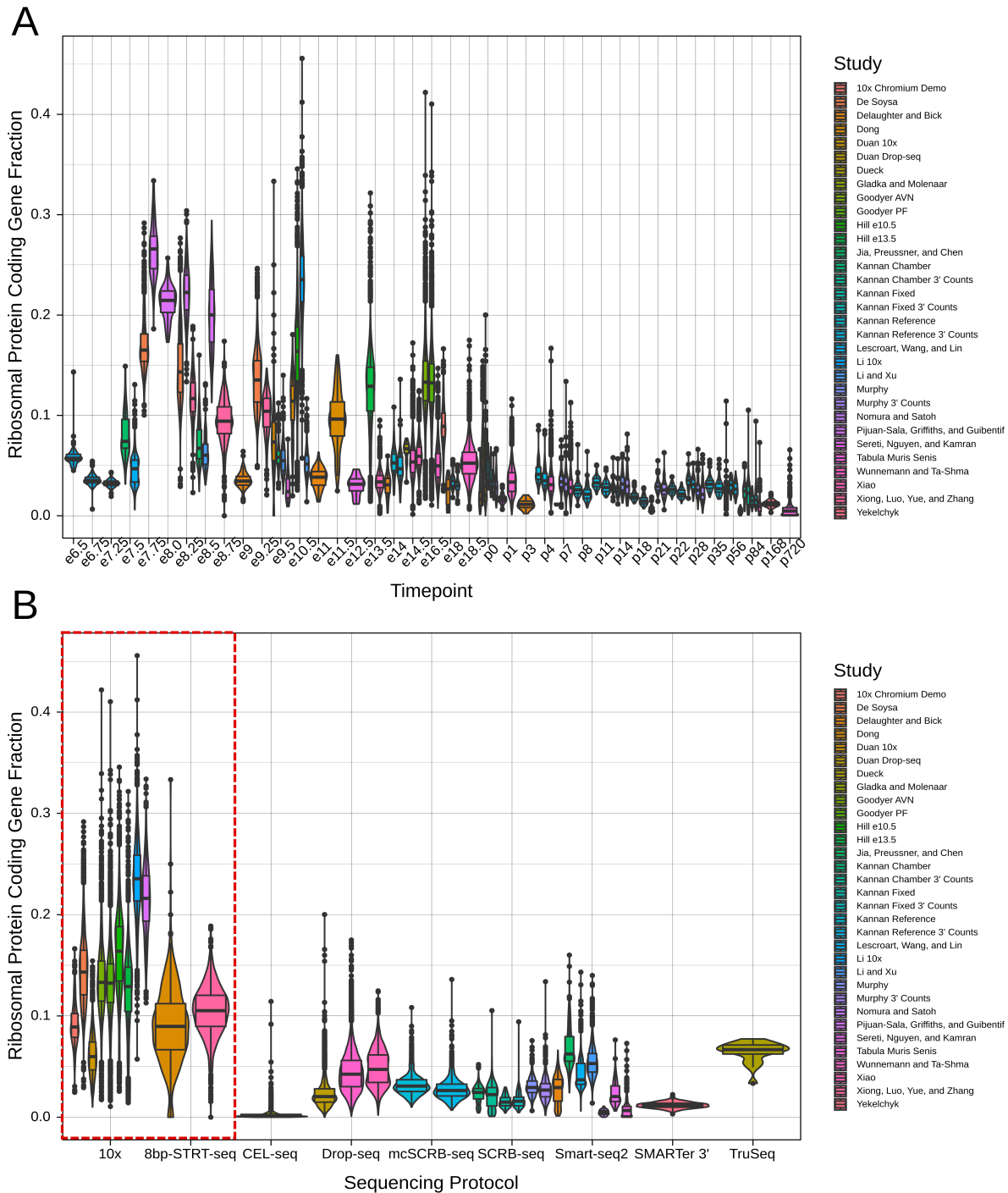


**Fig. S2. Ribosomal protein-coding genes are expressed in a sequencing protocol-specific manner. A.** Proportion of ribosomal protein coding genes in mouse *in vivo* datasets, grouped by timepoint. **B.** Proportion of ribosomal protein coding genes in mouse *in vivo* datasets, grouped by library preparation method. 10x v1-v3 protocols have been coalesced together for the purposes of this figure.

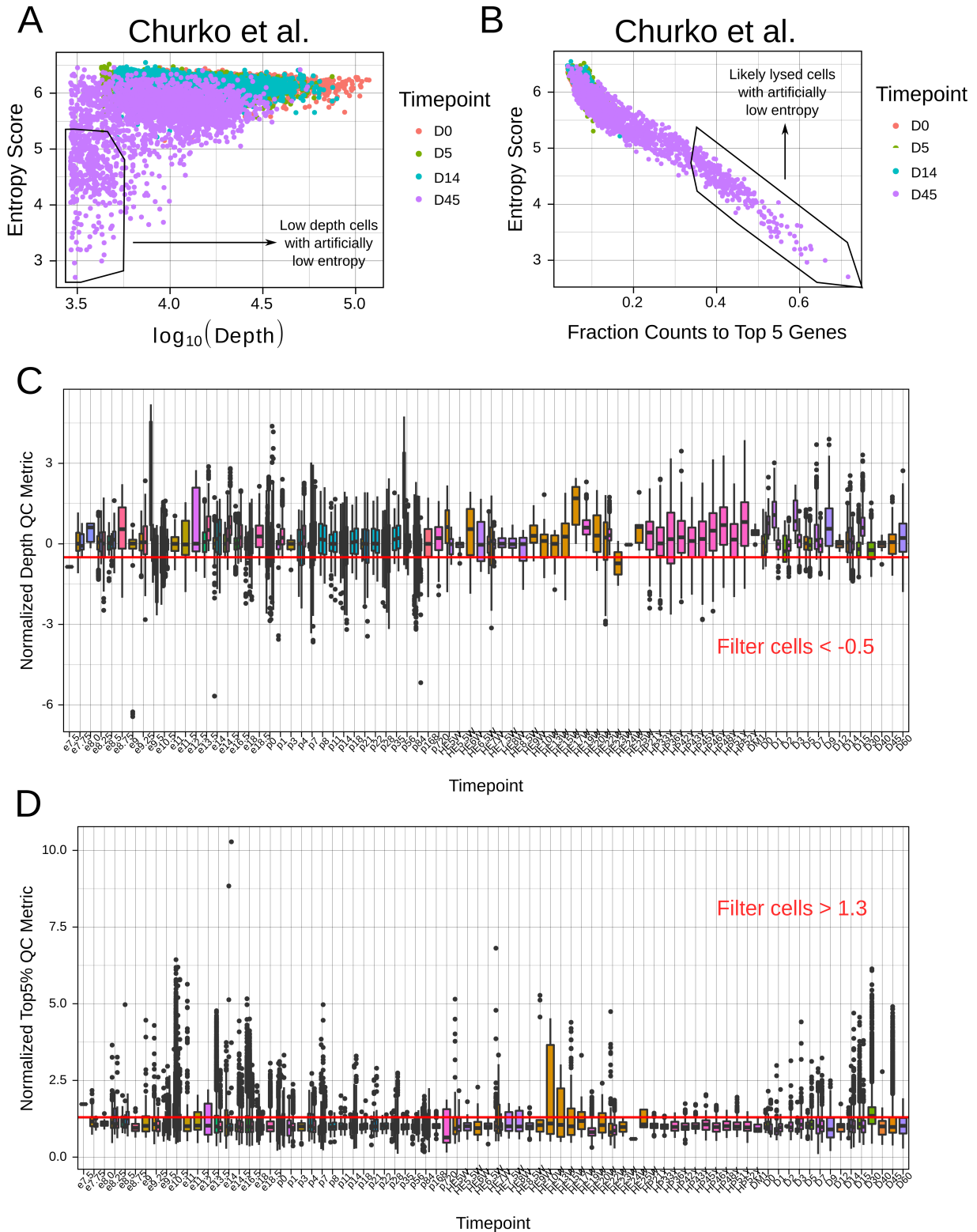


**Fig. S3. Poor quality single cells can be identified and removed with normalized depth and top 5 gene percentage metrics.** **A.** Example of unusually low entropy cells due to low depth in the Churko et al. dataset. **B.** Example of unusually low entropy cells due to high top 5 gene percentage in the Churko et al. dataset. **C.** Normalized depth QC metric for all datasets. Red line indicates the threshold of  $-0.5$ . **D.** Normalized top 5 gene percentage metric for all datasets. Red line indicates the threshold of  $1.3$ .

To identify such datasets, we used the percentage of mitochondrial reads as a quality control metric. We plotted the mitochondrial reads across all the mouse *in vivo* datasets in **Figure S4A**, highlighting datasets with unusually high mitochondrial percentage in red. We subsequently discarded these datasets (**Figure S4B**). The final relationship between timepoint and mitochondrial reads in mouse *in vivo* data, subsequent to eliminating low depth datasets (discussed in **Supplementary Note 6**), is shown in **Figure S4C**.

Currently, there is no automated approach for easily identifying poor quality datasets. The clear relationship between timepoint and mitochondrial reads in mouse datasets, as seen in **Figure S4C**, may help define better approaches in the future. However, the limited data available for *in vivo* human cardiac tissues makes it difficult to assess similarly for human CMs. We thus erred on the side of caution, and tried to avoid eliminating datasets without clear rationale for doing so. In some cases, we eliminated certain portions of datasets (for example, one patient or tissue region) if they appeared clearly irregular. However, these decisions were necessarily made on an *ad hoc* basis. We outlined our rationale for discarding any datasets in the **Appendix**, with the hope that transparency could suffice in the current absence of more rigorous dataset disqualification criteria.

**Supplementary Note 5: Identifying CMs.** In terms of cell-type filtration, our input datasets were fairly heterogeneous, with some including only CMs while others were more broad. Thus, we used SingleCellNet (12) to identify and retain only cells with CM signature. SingleCellNet uses top-scoring pair to enable cross-platform comparisons of test data against a training dataset to annotate celltypes, and has performed well in benchmarking (13). We used the Tabula Muris (14) as a reference dataset to test against many celltypes. However, as the Tabula Muris is constructed on adult tissues, we were concerned that early-stage CMs may be poorly classified. We thus tested the predicted cell annotations from SingleCellNet across our mouse *in vivo* datasets. We classified a cell as a CM if its score for “cardiac muscle cell” was higher than the score for any other celltype. We found that, while prediction scores for CMs increased over time, CMs were identified as early as e7.5, corresponding appropriately to the onset of cardiomyogenesis (**Figure S5A**). In human *in vivo* datasets, CMs were present by embryonic week 5, which was the earliest timepoint for which we had data (**Figure S5B**). These results supported the use of the Tabula Muris reference with SingleCellNet, even for identifying nascent CMs. We lastly tested the use of SingleCellNet on *in vitro* directed differentiation datasets. We found that cells with CM-like signature appeared by D5 of differentiation (**Figure S5C**), though we focused our analysis on D9 onwards.

**Supplementary Note 6: Robustness of entropy score.** We aimed to establish entropy score as a metric of CM maturation that could be effectively used for cross-study comparison. Entropy score must therefore be robust to parameters that will vary across studies. We demonstrated previously that after mitochondrial pseudogene correction, entropy score is robust to mapping/counting pipeline (**Figure S1, Supplementary Note 1**). We consider here the utility of entropy across sequencing protocols and across a range of sequencing depths.

To test entropy score on multiple sequencing protocols, we used data from the benchmarking of six scRNA-seq protocols with mouse embryonic stem cells (15). This dataset was optimal for comparison because 1) it utilized one, well-defined celltype; 2) tested a range of protocol types; and 3) sequenced all protocols to high depth, thereby eliminating depth as a confounder. All of the protocols generated similar entropy scores with the exception of CELseq2 (**Figure S6A**). However, this may have been due to an error in the running of this particular protocol, as the CELseq2 samples presented with unusually high mitochondrial percentage (**Figure S6B**). The remaining protocols covered a range of characteristics, including plate-based, droplet-based, and microfluidic approaches, supporting the use of entropy score regardless of sequencing protocol used to generate the data.

We next wished to test entropy score across different depths. The achieved depth of a particular dataset is dependent on a number of characteristics, including sensitivity of the sequencing protocol, number of cells sequenced, and the choice of sequencing machine/lane, which may in turn be affected by many experiment-specific considerations (15–17). We selected four datasets with a range of baseline depths, and performed subsampling to determine a minimum required depth for accurate entropy quantifications. We defined accuracy based on the deviation from the baseline entropy score, and set a threshold of 98% accuracy (corresponding  $\sim 0.1$  change in entropy score). Entropy score was relatively robust to subsampling, with 98% accuracy being achieved at above  $\sim 2000$ – $4500$  counts/cell, depending on the dataset (**Figure S7**). While this depth was sufficient for most of our assayed datasets, some very low-depth datasets were affected - in particular, all four Drop-seq datasets tested had depths ranging from 1500 - 4100 counts/cell. Perhaps relatedly, these Drop-seq datasets often had unusually high entropy compared to other datasets at the same timepoint. As a particularly striking example, the Drop-seq data from Duan et al. had a 10% increase in entropy score from the 10x data produced by the same group. While **Figure S6A** indicates that high-depth Drop-seq should be comparable to data generated by other protocols, it is likely that low-depth Drop-seq poorly captures very highly expressed genes. Given these results, we omitted the Drop-seq datasets from further analysis. We additionally advise users of entropy score to sequence samples to at least 5000 counts per cell.

**Other Supplementary Figures.** In addition to the supplementary figures discussed above, we include here **Figures S8-S11**. **Figure S8** shows entropy scores for *in vivo* datasets as in **Figure 2B**, but labeled by different characteristics. **Figure S9** shows the attempted integration of several perinatal datasets by Seurat. **Figure S10** shows the ratio of entropy scores computed on four UMI datasets pre- and post-UMI collapsing. **Figure S11** shows trajectory inference of our maturation reference using Monocle 2, Slingshot, and SCORPIUS, as well as the correlation to entropy score for each method. **Figure S12** show gene expression trends across entropy, as in **Figure 3C**, for three one-timepoint datasets. Further details for each can be found in the corresponding captions, as well as our publicly available code.

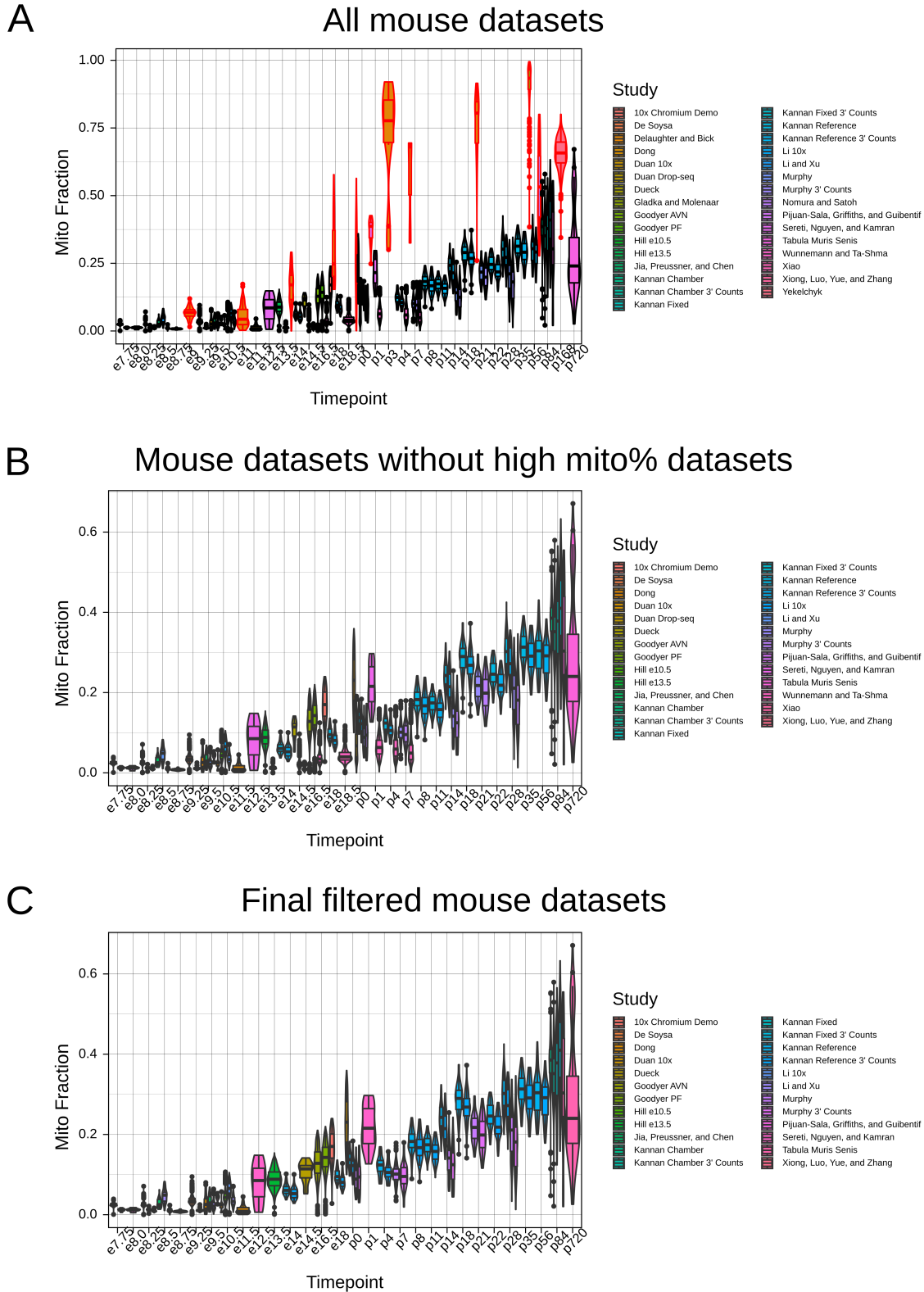


**Fig. S4. Poor quality datasets can be identified on an *ad hoc* basis with mitochondrial gene proportion.** **A.** Mitochondrial gene proportions in mouse *in vivo* datasets. Datasets with unusually high proportions are highlighted in red. **B.** As in **A**, but with high mitochondrial proportion datasets removed. **C.** Mitochondrial proportions for mouse *in vivo* datasets included in final analysis (as in **B**, but with low depth datasets removed).

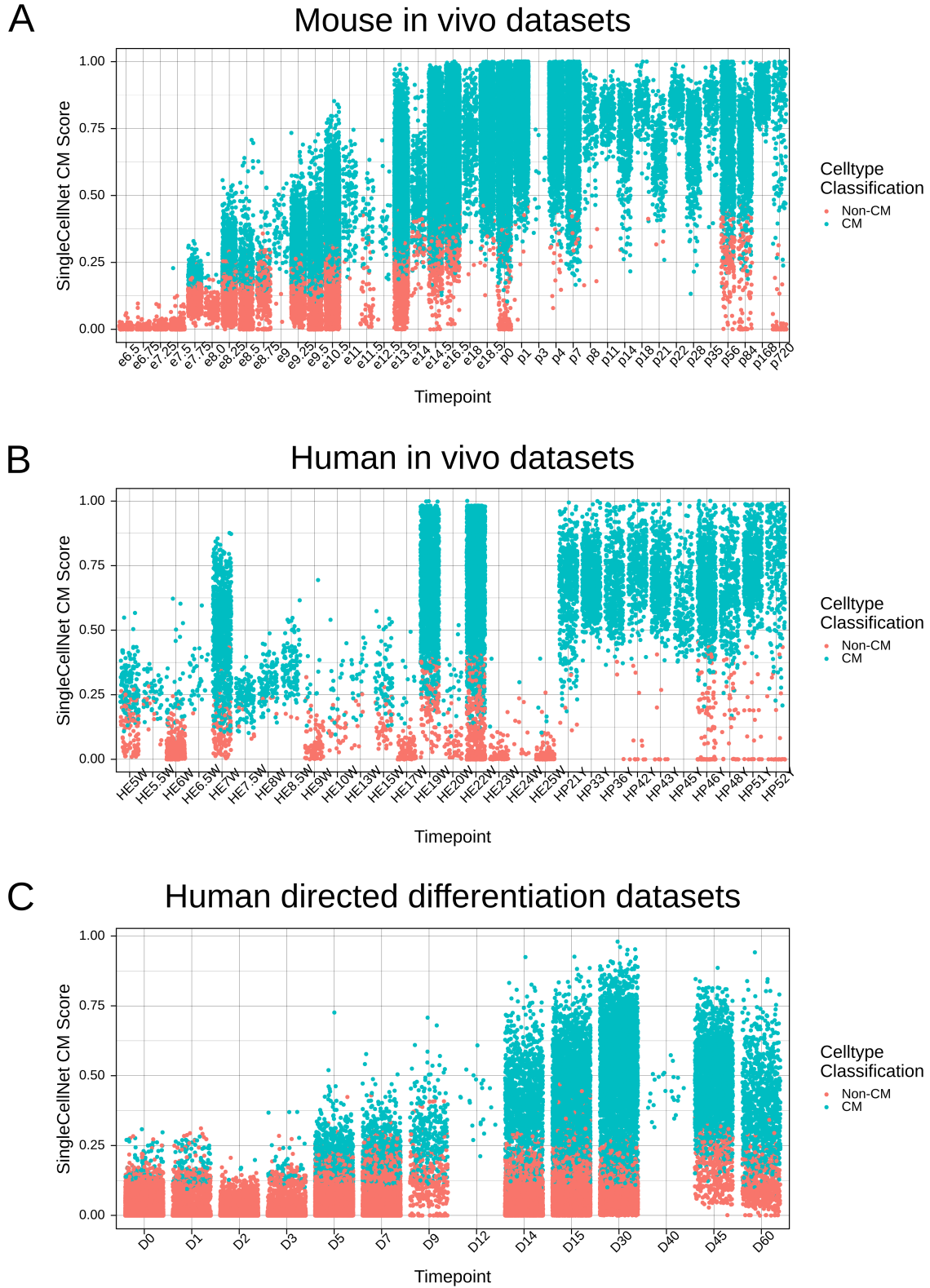


**Fig. S5. SingleCellNet identifies single cells with CM signature.** **A.** SingleCellNet CM scores for mouse *in vivo* datasets by timepoint. Cells are labeled based on whether their highest classification was for "cardiac muscle" or another celltype. **B.** As above, for human *in vivo* datasets. **C.** As above, for human *in vitro* directed differentiation datasets.

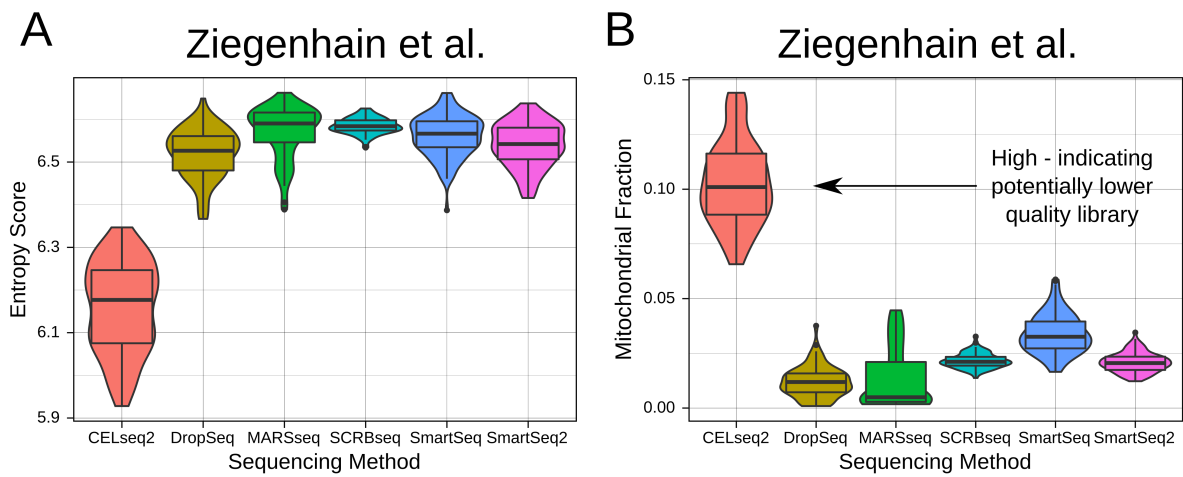


**Fig. S6. Entropy score is consistent across sequencing protocols.** **A.** Entropy score computed for mouse embryonic stem cells for six different library preparation methods from Ziegenhain et al. For this figure, the SingleCellNet filter was not used. **B.** Mitochondrial proportions for the above dataset.

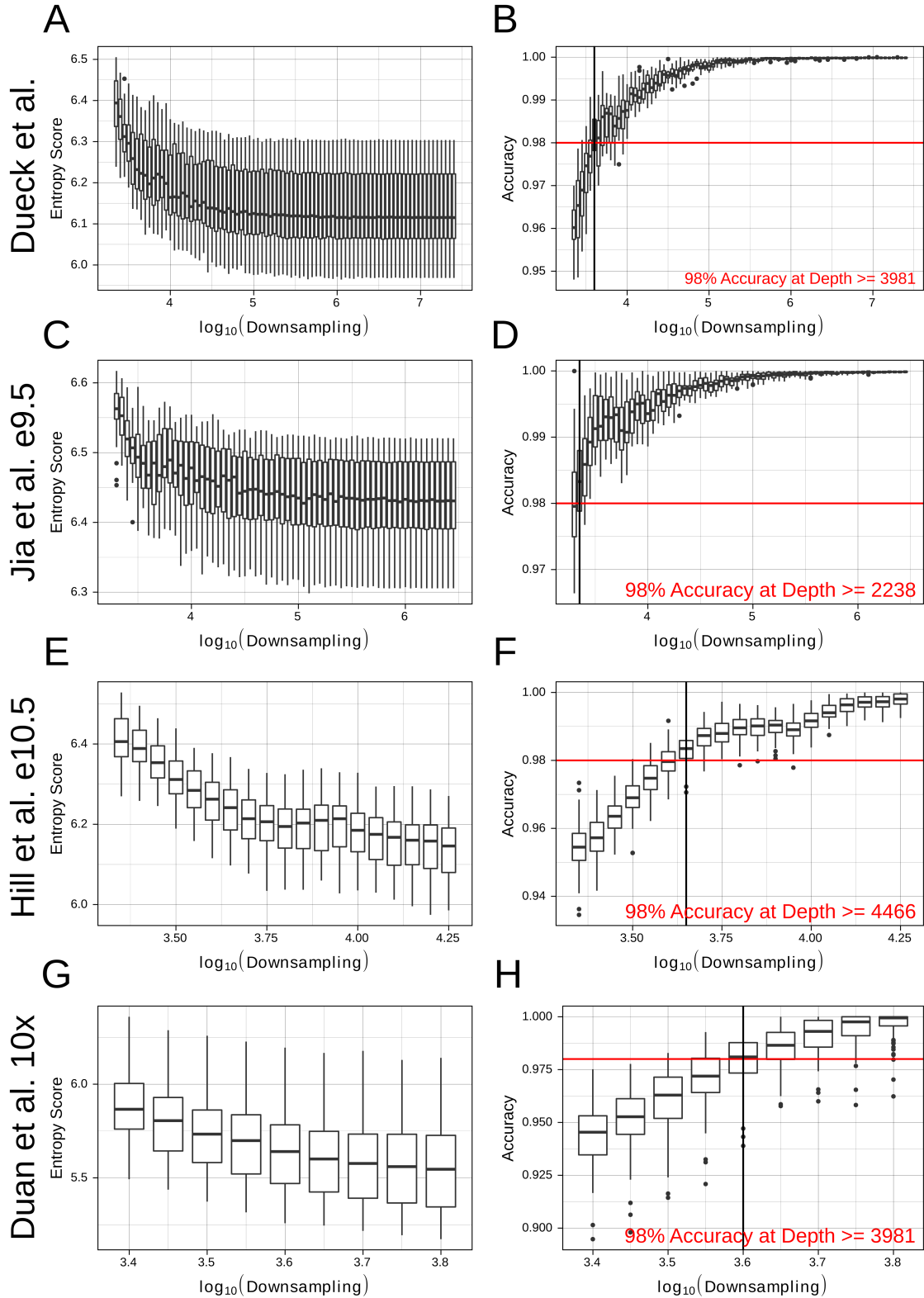


**Fig. S7. Entropy score is robust across a range of sequencing depths.** For each of four datasets, we performed subsampling and computed the entropy score as well as accuracy (calculated as deviation from baseline entropy score). At each stage, we included only cells with genes > 1000, and subsampled only to a depth where the median number of genes remained > 1000. Data is shown for **A-B**. Dueck et al. **C-D**. Jia et al. at e9.5. **E-F**. First 100 cells from Hill et al. at e10.5. **G-H**. First 100 cells from Duan et al.

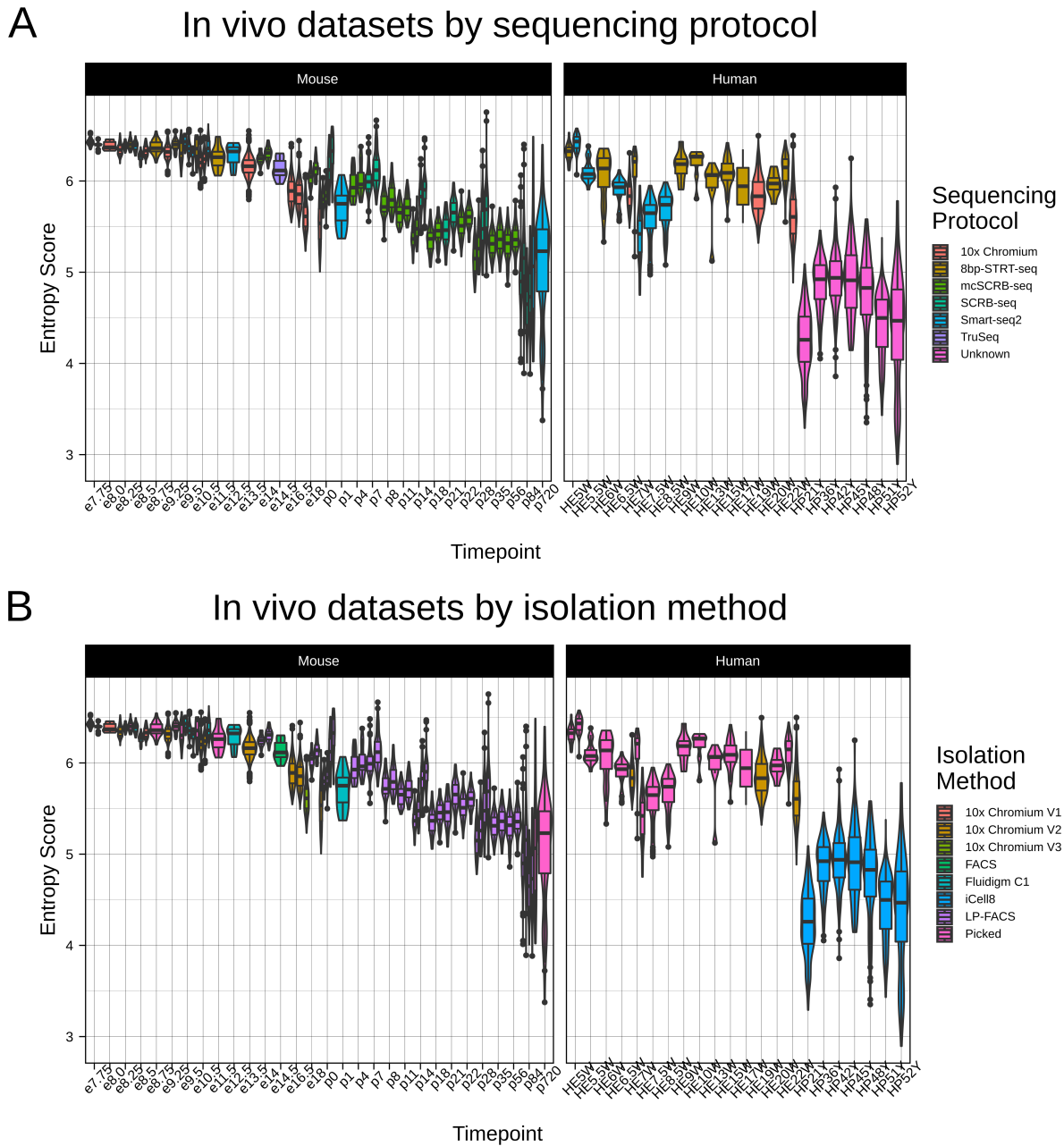


**Fig. S8. Entropy score enables comparison of maturation status of CMs from scRNA-seq datasets with diverse characteristics.** This figure corresponds to **Figure 2B**, but with boxplots coloured by **A.** sequencing protocol and **B.** isolation method.

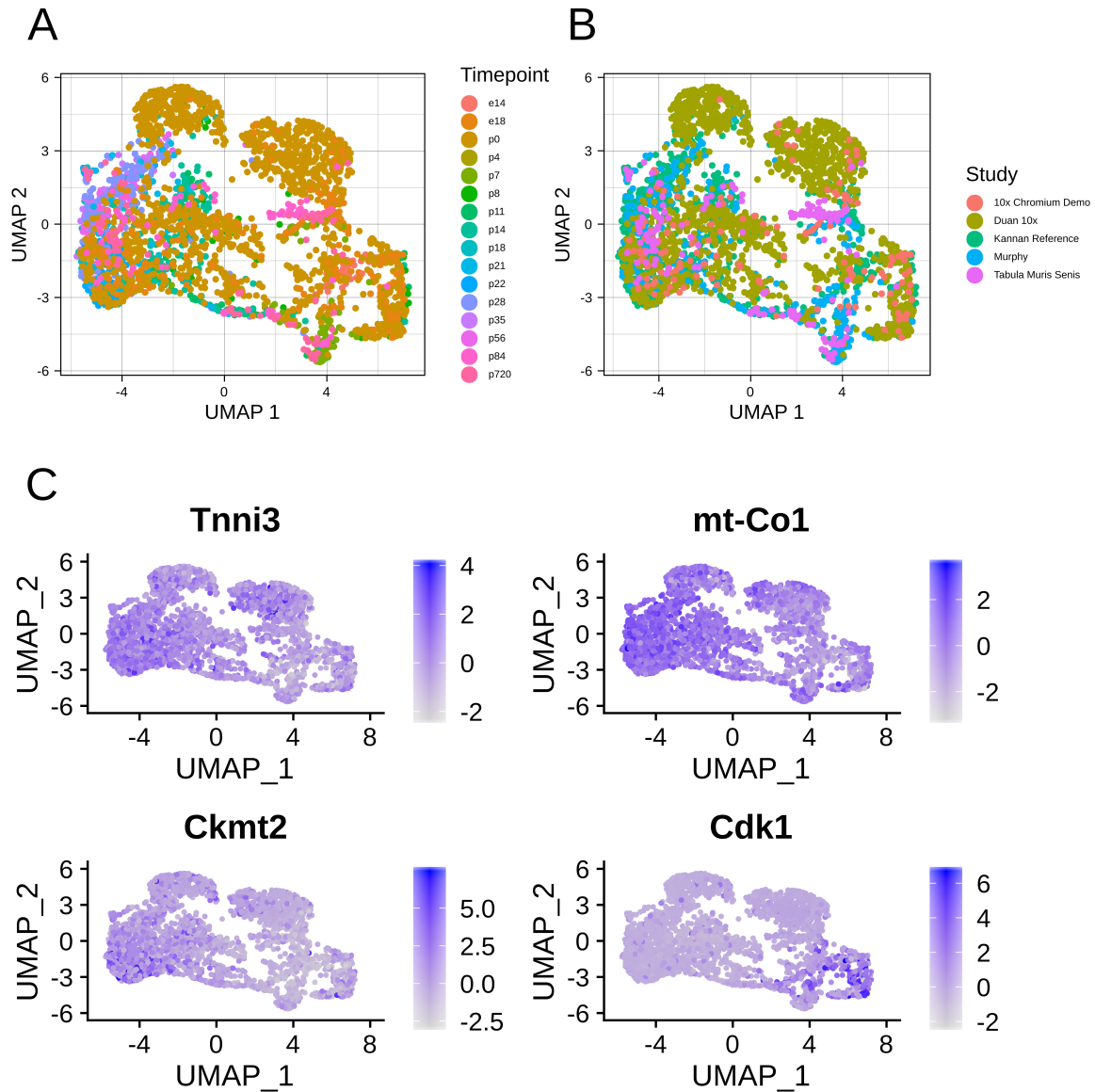


**Fig. S9. Batch effects between datasets with overlapping timepoints are only partially corrected by integration methods.** We used Seurat v3 to integrate 5 datasets with perinatal timepoints, using SCTransform for normalization and our maturation reference dataset as a reference for integration. **A.** UMAP plot of integrated datasets labeled by timepoint. **B.** UMAP plot of integrated datasets labeled by dataset. **C.** Integrated UMAP plot coloured by gene expression of four maturation-related genes.

A

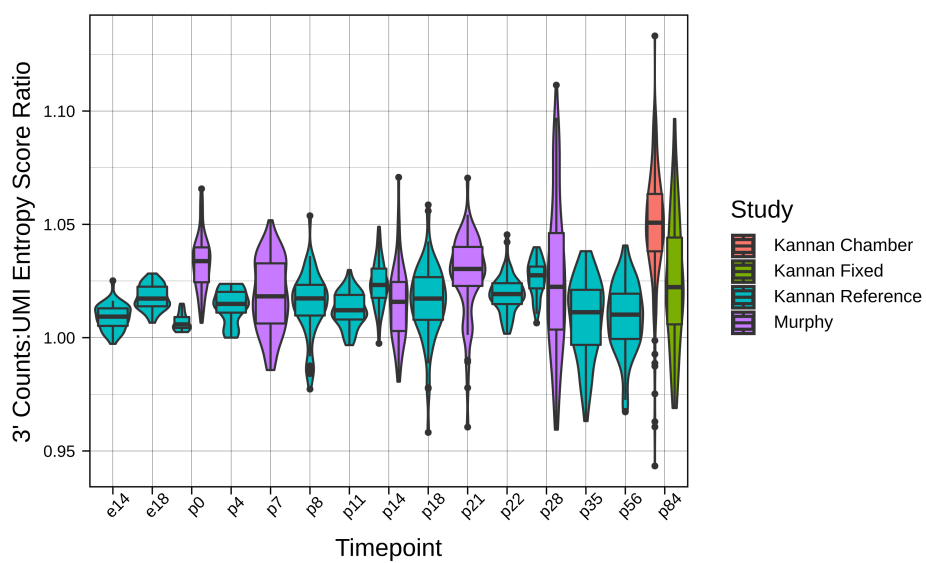
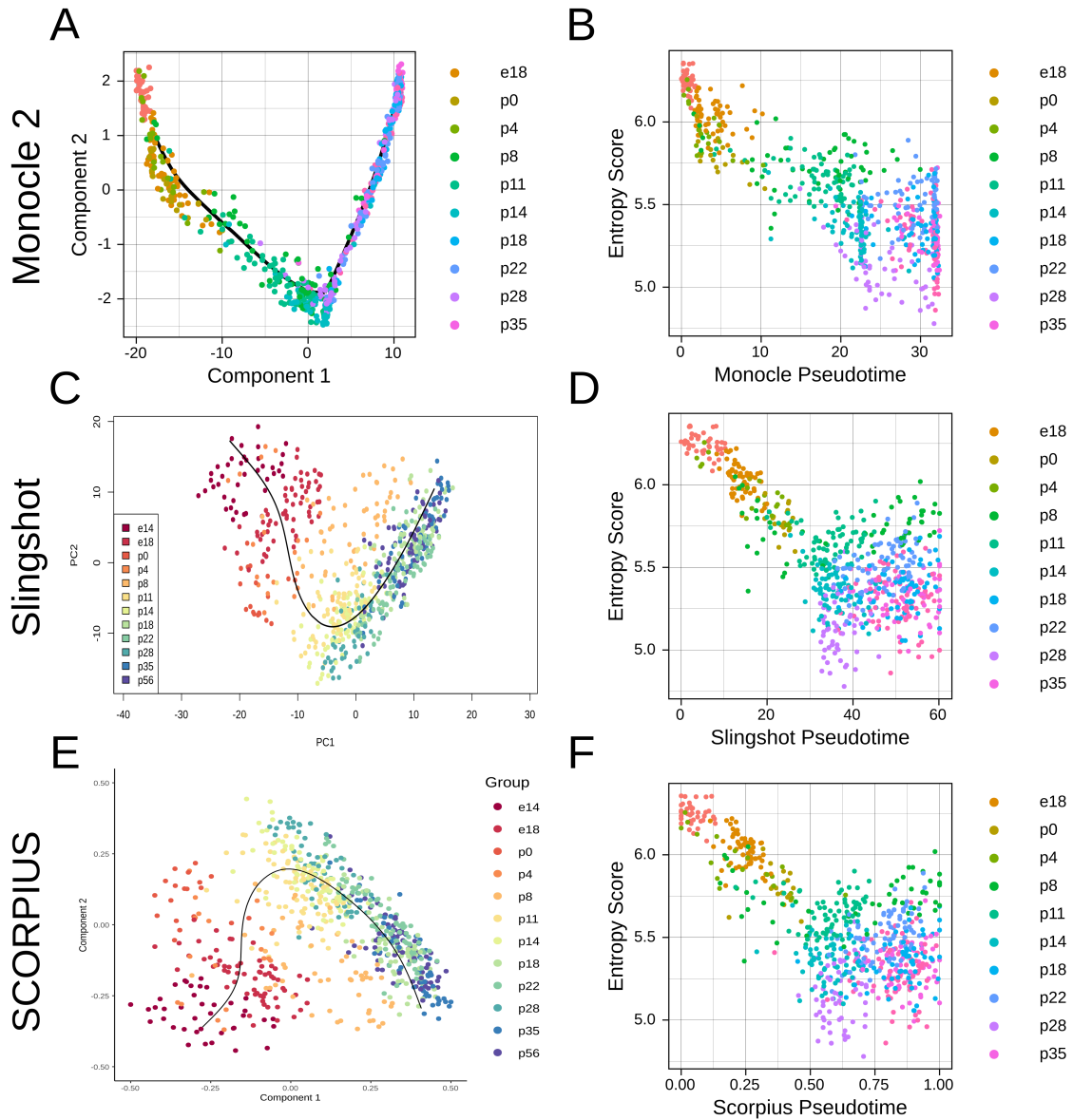
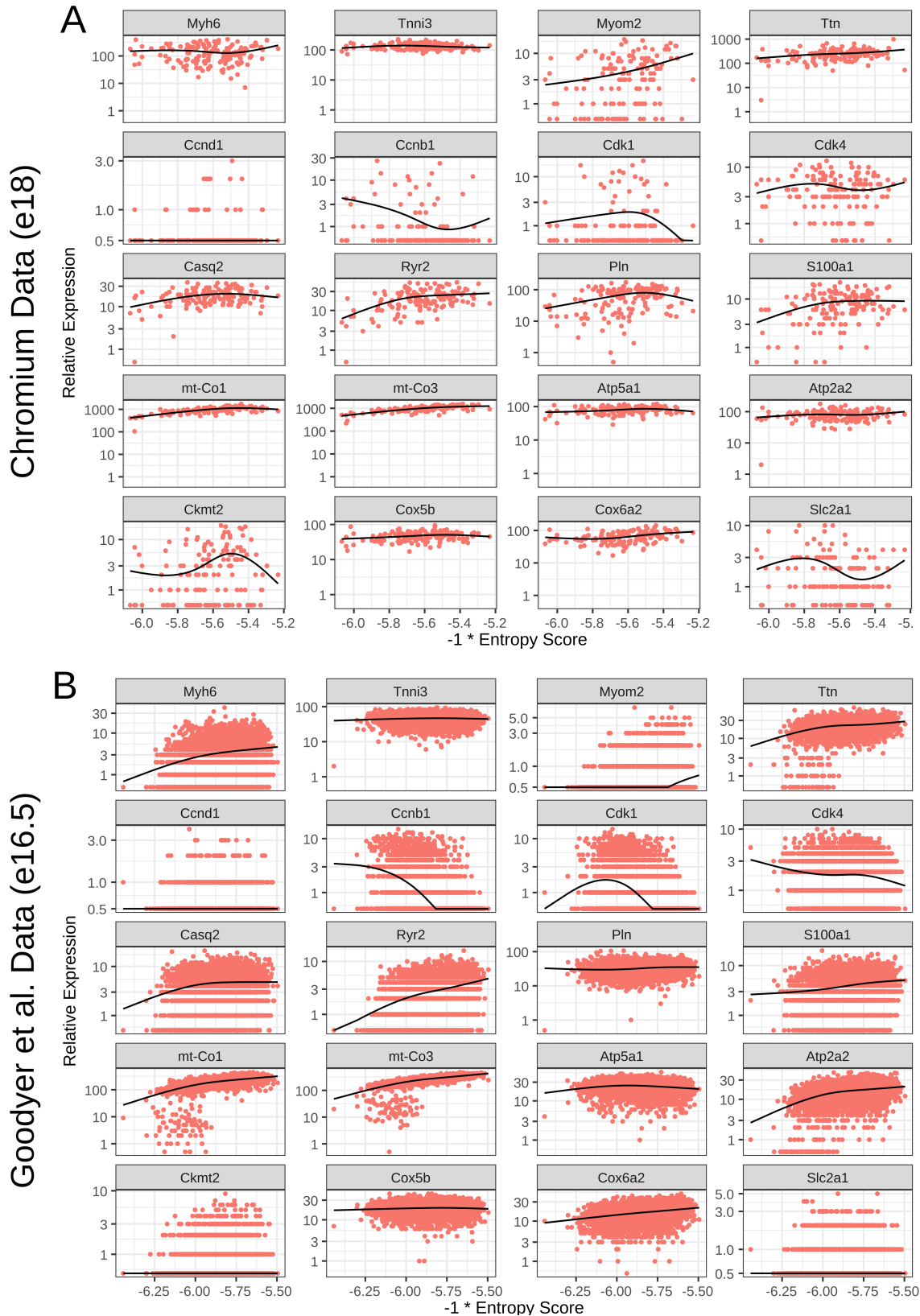


Fig. S10. Entropy score is consistent for UMI datasets pre- and post-UMI collapsing. A. Ratio of entropy score for UMI datasets computed prior to vs. after UMI collapsing.



**Fig. S11. Entropy score correlates modestly with previous trajectory inference methods.** We reconstructed trajectories of our maturation reference dataset using **A-B.** Monocle 2, **C-D.** Slingshot, and **E-F.** SCORPIUS.



**Fig. S12. Entropy score captures CM maturation-related gene expression trends in one-timepoint datasets.** Gene trends across entropy score, as in **Figure 3C**, are plotted for **A**. 10x Chromium heart dataset, **B**. Goodyer et al., and **C**. Duan et al. *Figure continues on next page.*

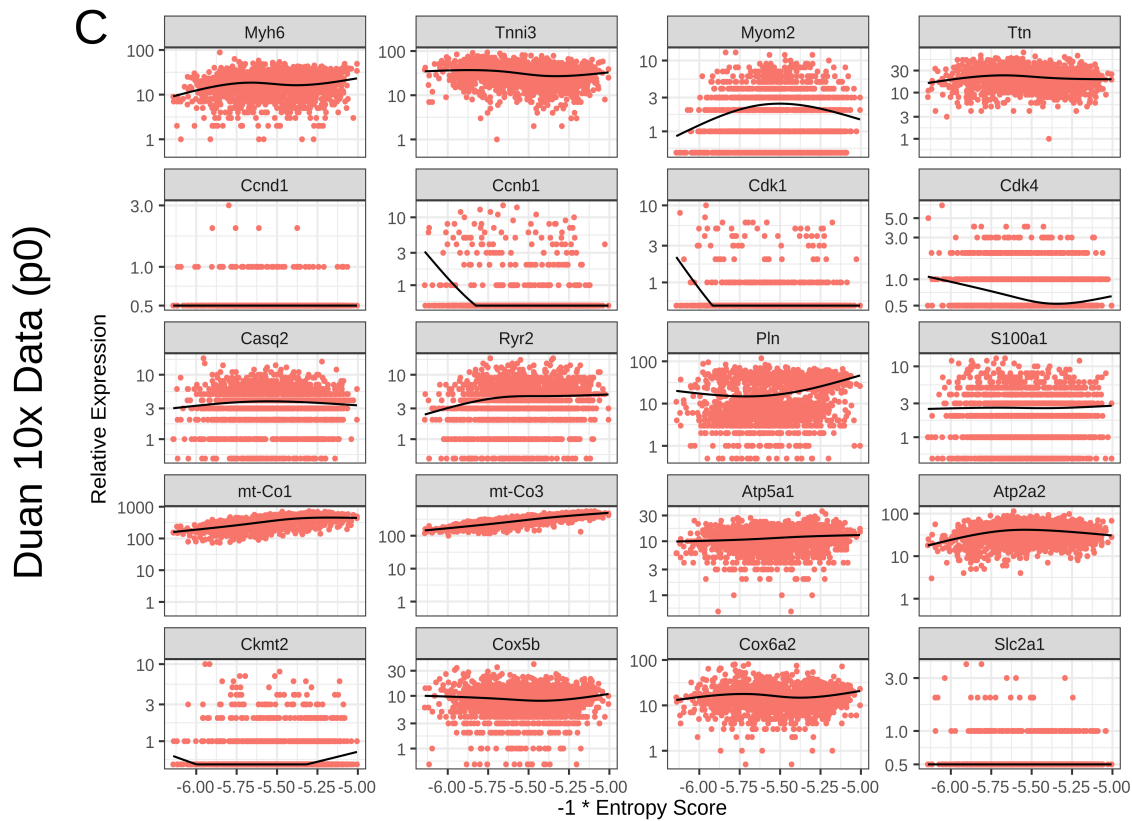


**Fig. S12.** Continued from previous page. **C.** Gene expression trends for Duan et al.

## Supplementary Methods

**Mice.** To generate mice for our reference dataset, we crossed B6.FVB-Tg(Myh6-cre)2182Mds/J mice (aMHC-cre, Jackson Laboratory, Stock No. 011038) with B6.129(Cg)-Gt(ROSA)26Sor<sup>tm4</sup>(ACTB-tdTomato,-EGFP)<sup>Luo</sup>/J (mTmG, Jackson Laboratory, Stock No. 007676). Both mice have C57BL/6J congenic background. All animals were maintained compliant to protocols by the Johns Hopkins Animal Care and Use Committee.

**CM Isolation.** For isolation of CMs from e14-p4 timepoints, we used the neonatal cardiomyocyte isolation kit from Miltenyi Biotec in conjunction with the gentleMACS Dissociator. For later timepoints, we performed Langendorff isolation of CMs. We prepared the following buffers:

- Perfusion buffer: 120 mM NaCl, 5.4 mM KCl, 1.2 mM NaH<sub>2</sub>PO<sub>4</sub>, 20 mM NaHCO<sub>3</sub>, 5.5 mM glucose, 5 mM BDM, 5 mM Taurine, and 1 mM MgCl<sub>2</sub>, adjusted to pH 7.4
- Digestion buffer: 40 mL Perfusion buffer plus 35.8 mg Collagenase Type II (Worthington CLS-2), 3 mg Protease (Sigma P5147)
- Tyrode's buffer: 140 mM NaCl, 5 mM KCl, 10 mM HEPES, 5.5 mM glucose, and 1 mM MgCl<sub>2</sub>, adjusted to pH 7.4

We used a horizontal (i.e. non-hanging) Langendorff apparatus with a chamber filled with perfusion buffer. To perform isolation, we first performed isoflurane anaesthesia on non-heparinized mice. Mice were observed until clearly anaesthetized and unresponsive to toe pinch, and subsequently euthanized by cervical dislocation. The heart was then rapidly excised from the chest and cannulated to the Langendorff apparatus. Flow time and rate of flow were dependent on the age of the mouse and were typically judged based on completeness of digestion to touch. Subsequently, the left ventricular free wall was excised and minced. We filtered isolated cells through a 100  $\mu$ M screen to eliminate large tissue chunks, spun down at 800 RPM for 1 minute (Eppendorf centrifuge 5702), and resuspended cells in 10 mL Tyrode's buffer.

**LP-FACS.** We have detailed our LP-FACS approach previously (5). We reproduce our methods here. We utilized a COPAS SELECT instrument (Union Biometrica). The COPAS SELECT was updated and rebranded as the FP-500, but the protocol here study does not use the new features and thus the two are functionally indistinguishable. We optimized sorting for cardiomyocytes by using a sort delay of 8 and sort width of 6. Additionally, we used the following fluorescence settings: ext

gain 50, green gain 200, yellow gain 200, red gain 255, extension integral gain 50, green integral gain 200, yellow integral gain 200, red integral gain 255, green PMT 800, yellow PMT 800, red PMT 1100. Coincidence check was selected to ensure proper single event sorting. We typically flowed cells between 20 - 60 events/second. We maintained cells in Tyrode's buffer during the sort and sorted them into Tyrode's buffer. To run the machine, we used ClearSort Sheath Fluid (Sony, Lot 1218L345).

**scRNA-seq Library Preparation and Sequencing.** We performed sequencing using the mcSCRIB-seq protocol (18). The protocol has been described at protocols.io at [dx.doi.org/10.17504/protocols.io.p9kdr4w](https://dx.doi.org/10.17504/protocols.io.p9kdr4w). Pooled libraries were sequenced on one mid-output lanes of the Illumina NextSeq500 with 16 base pair barcode read, 8 base pair i7 index read, and 66 base pair cDNA read design.

**Computational Analyses.** All analyses performed in the paper were done in R; code to reproduce the figures can be found at our Github (<https://github.com/skannan4/cm-entropy-score>). Dataset characteristics are presented in **Supplementary Tables 1 and 2**, and details of each individual dataset are described in the **Appendix**. Differential gene expression analysis for **Figures 2C and 2D** were done using Monocle 2, replacing Monocle 2's generated pseudotime with entropy score or pseudotime from other methods as appropriate.

## Appendix

This appendix contains information about all of the datasets included for analysis in the study, including how they were acquired and processed. Metrics for each dataset are provided in **Supplementary Tables 1 and 2**. We have relevant data on Github at <https://github.com/skannan4/cm-entropy-score>. This includes an R workspace containing counts table for every dataset in this study, an R workspace containing just the final processed calculations (for lower memory usage), code for functions relevant to usage of entropy score, and code to reproduce the figures in the manuscript. If any additional information is required, we encourage direct inquiries and aim to respond as soon as possible.

### Mouse In Vivo.

#### *10x Chromium*

##### *10k Heart Cells from an E18 mouse (v3 chemistry)*

We downloaded the filtered feature/cell matrix from the 10x chromium datasets website ([https://support.10xgenomics.com/single-cell-gene-expression/datasets/3.0.0/heart\\_10k\\_v3?](https://support.10xgenomics.com/single-cell-gene-expression/datasets/3.0.0/heart_10k_v3?)). We subsequently performed UMAP + clustering using Seurat and selected the healthy cardiomyocytes as the cluster clearly expressing cardiomyocyte markers and having comparable/higher read/gene counts to other clusters.

##### *T. Yvanka de Soysa et al. (Casey Gifford, Deepak Srivastava)*

##### *Single-cell analysis of cardiogenesis reveals basis for organ-level developmental defects*

We pulled the UMI data from the tables uploaded by the authors at GEO (GSE126128), selecting only wild-type cells at all available timepoints. We used the annotations provided by the authors as the source data to Extended Data Figure 1 to identify tissue, and selected out cells labeled as "myocardium." We used the annotations provided by the authors as source data to Extended Figure 1 to annotate myocardial region, though we did not filter based on these annotations.

##### *Daniel DeLaughter and Alexander Bick et al. (Jonathan Seidman, Christine Seidman)*

##### *Single-Cell Resolution of Temporal Gene Expression during Heart Development*

We pulled the FastQ data from the authors' private database (<https://b2b.hci.utah.edu/gnomex/>) and mapped using STAR/FeatureCounts. We then performed T-SNE + clustering through Seurat and selected healthy cardiomyocytes as the clusters clearly expressing cardiomyocyte markers. However, we found that this data consistently had higher mitochondrial percentage at almost every timepoint compared to other datasets (most notably in the perinatal and postnatal timepoints). Thus, we discarded this dataset.

##### *Ji Dong et al. (Fuchou Tang)*

##### *Single-cell RNA-seq analysis unveils a prevalent epithelial/mesenchymal hybrid state during mouse organogenesis*

The uploaded data of the authors does not contain mitochondrial reads. Therefore, we pulled and mapped the FastQ data from the four heart samples from ENA (PRJNA343327) using the FASTerQ approach with Kallisto|Bustools. Read 1 was used as the cDNA read (base pairs 45 to 140, to avoid potential adaptor and poly A tails), while Read 2 was used for barcode (first 8 bp) and UMI (second 8 bp). Because of the short UMI length, we found that Kallisto|Bustools discarded many UMIs during counting. We thus used a custom script to count UMIs from the Kallisto|Bustools output.

##### *Jialei Duan et al. (Nikhil Munshi, Gary Hon)*

##### *Rational Reprogramming of Cellular States by Combinatorial Perturbation*

The UMI data was pulled from the tables uploaded by the authors at GEO (GSE117795). We collated all of the in vivo samples, with the 10x and Drop-seq data being handled separately. We then performed UMAP + clustering through Seurat and selected healthy cardiomyocytes as the clusters clearly expressing cardiomyocyte markers while having comparable read counts to other

clusters and comparable mitochondrial percentage (discarding clusters with notably high mitochondrial percentage or low genes). We could readily distinguish atrial and ventricular myocytes using myosin light chain isoforms, and annotated the cells accordingly. We found that the Drop-seq data had unusually high entropy, something we observed across multiple Drop-seq datasets (and perhaps owing to low depth); thus, we discarded the Drop-seq data.

*Hannah Dueck et al. (Junhyong Kim)*

*Deep sequencing reveals cell-type-specific patterns of single-cell transcriptome variation*

The uploaded data of the authors does not contain mitochondrial reads. Therefore, we pulled the FastQ data from the cardiomyocyte samples from ENA (PRJNA244374) and then mapped with Kallisto (pseudo in batch mode with the -quant flag).

*Monika Gladka and Bas Molenaar et al. (Eva von Rooij)*

*Single-Cell Sequencing of the Healthy and Diseased Heart Reveals Cytoskeleton-Associated Protein 4 as a New Modulator of Fibroblasts Activation*

Counts tables were kindly provided by the authors. We used UMAP + clustering through Seurat to select cardiomyocytes based on clusters expressing cardiomyocyte markers. We observed, however, that the dataset had very high mitochondrial percentages, often close to 90%. We thus discarded this dataset.

*William Goodyer (Sean Wu)*

*Transcriptomic Profiling of the Developing Cardiac Conduction System at Single-Cell Resolution*

We pulled the UMI data from tables uploaded by the authors at GEO (GSE132658). The authors kindly provided us with the clustering used in the manuscript, which we used to select out cardiomyocytes. We used the PF (left and right) and AVN datasets as the metadata was not available for the SAN data.

*Matthew Hill et al. (James Martin)*

*A cellular atlas of Pitx2-dependent cardiac development*

The UMI data was pulled from the tables uploaded by the authors (GSE131181), and the metadata tables were pulled from the same source. We used the authors' generated clusters and selected clusters with high expression of cardiomyocyte markers. We subsequently selected only control cells from both timepoints.

*Guanshuai Jia, Jens Preussner, and Xi Chen et al. (Thomas Braun)*

*Single cell RNA-seq and ATAC-seq analysis of cardiac progenitor cell transition states and lineage settlement*

The counts data was pulled from the authors' Github (<https://github.com/loosolab/cardiac-progenitors>). We used the data from both Isl and Nkx GFP lines.

*Suraj Kannan et al. (Chulan Kwon)*

*Large Particle Fluorescence-Activated Cell Sorting Enables High-Quality Single-Cell RNA Sequencing and Functional Analysis of Adult Cardiomyocytes*

This data was generated at our lab and is available at GEO (GSE133640). We used both the multi-chamber study and the lived/fixed study and included all cells from both studies. Both 3' counts and UMIs (output from zUMIs, using intronic and exonic reads) were used for analysis.

*Suraj Kannan et al. (Chulan Kwon)*

*Transcriptomic entropy quantifies cardiomyocyte maturation at single cell level*

This data (described in this manuscript) was generated at our lab and is available at GEO (GSE147807). Both 3' counts and UMIs (output from zUMIs, using intronic and exonic reads) were used for analysis.

*Fabienne Lescroart, Xiaonan Wang, and Xionghui Lin et al. (Cedric Blanpain)*

*Defining the earliest step of cardiovascular lineage segregation by single-cell RNA-seq*

We download the counts data from the author's private website (<http://singlecell.stemcells.cam.ac.uk/mesp1#data>). We subsequently selected only wild-type cells.

*Guang Li and Adele Xu et al. (Sean Wu)*

*Transcriptomic Profiling Maps Anatomically Patterned Subpopulations among Single Embryonic Cardiac Cells*

We pulled the counts data uploaded by the authors at GEO (GSE76118). We subsequently performed TSNE + clustering through Seurat and selected clusters clearly identifiable as cardiomyocytes by marker gene expression. We selected all wild-type cells, including from the Nkx experiment.

*Guang Li et al. (Sean Wu)*

*Single cell expression analysis reveals anatomical and cell cycle-dependent transcriptional shifts during heart development*

We pulled the UMI data uploaded by the authors at GEO (GSE122403). We subsequently performed UMAP + clustering through Seurat and selected clusters clearly identifiable as cardiomyocytes by marker gene expression.

*Sean Murphy et al. (Chulan Kwon)*

*Single-Cell Analysis Identifies PGC1 as a Master Regulator of Cardiomyocyte Maturation*

This data was generated in our lab; the raw data is currently not publicly available, but will be shortly. We selected only the wild-type cardiomyocytes for further analysis. Both 3' counts and UMIs (output from zUMIs, using intronic and exonic reads) were used for analysis.

*Seitaro Nomura and Masahiro Satoh et al. (Hiroyuki Aburatani, Issei Komuro)*

*Cardiomyocyte gene programs encoding morphological and functional signatures in cardiac hypertrophy and failure*

The uploaded data of the authors does not contain mitochondrial reads. Therefore, we pulled and mapped the FastQ data from the sham cardiomyocytes from ENA (PRJNA376183) using STAR/FeatureCounts. However, we found that the dataset had a high percentage of mitochondrial reads; thus, we discarded this dataset.

*Blanca Pijuan-Sala, Jonathan Griffiths, and Caroline Guibentif et al. (John Marioni and Berthold Gottgens)*

*A single-cell molecular map of mouse gastrulation and early organogenesis*

We pulled the UMI data following the instructions from the authors' Github page

(<https://github.com/MarioniLab/EmbryoTimecourse2018/blob/master/download/download.sh>). We subsequently used the authors' labelings to select cells classified as "Cardiomyocyte."

*Konstantina-Ioanna Sereti, Ngoc Nguyen, and Paniz Kamran et al. (Reza Ardehali)*

*Analysis of cardiomyocyte clonal expansion during mouse heart development and injury*

The uploaded data of the authors does not contain mitochondrial reads. Therefore, we pulled the FastQ data from ENA (PRJNA427266) and remapped using Kallisto (pseudo in batch mode with the -quant flag). We found the p1 timepoint to be bimodal in terms of mitochondrial gene expression. However, because of the relatively small cell number and large fraction of poor quality cells, we found that our top5 filter did not catch all low quality cells. We thus also excluded all p1 cells with >30% mitochondrial reads.

*Tabula Muris Consortium*

*A Single Cell Transcriptomic Atlas Characterizes Aging Tissues in the Mouse*

We pulled the BAM files for the Fluidigm studies from the publicly available AWS bucket

(<https://registry.opendata.aws/tabula-muris-senis/>) and the annotations from the authors' Figshare

([https://figshare.com/projects/Tabula\\_Muris\\_Senis/64982](https://figshare.com/projects/Tabula_Muris_Senis/64982)). Specifically, for the latter, we used the metadata stored in the scanpy object, and matched the names of cells between this annotation and the raw data available through AWS. We focused only on the Fluidigm data for our study. We subsequently selected all cells from the "heart" tissue category. As we were unsure of the settings used to count with HTSeq, we recounted from the BAM files using FeatureCounts.

*Florian Wunnemann and Asaf Ta-Shma et al. (Gregor Andelfinger)*

*Loss of ADAMTS19 causes progressive non-syndromic heart valve disease*

Counts table and metadata were kindly provided by the authors. We used UMAP + clustering through Seurat to select cardiomyocytes based on clusters expressing cardiomyocyte markers and having comparable read and gene counts to other clusters. We additionally annotated clusters as atrial or ventricular, though we analyzed both sets of cells. However, as with several other Drop-seq datasets, we found that the data had unusually high entropy (and perhaps owing to low depth); thus, we discarded this dataset.

*Yang Xiao et al. (James Martin)*

*Hippo Signaling Plays an Essential Role in Cell State Transitions during Cardiac Fibroblast Development*

We pulled the UMI data uploaded by the authors are GEO (GSE100861). The metadata was kindly provided by the authors, and included the clustering used in the manuscript. We selected wild-type cells in the cardiomyocyte cluster. However, as with several other Drop-seq datasets, we found that the data had unusually high entropy (and perhaps owing to low depth); thus, we discarded this dataset.

*Haiqing Xiong, Yingjie Luo, Yanzhu Yue, and Jiejie Zhang et al. (Albin He)*

*Single-Cell Transcriptomics Reveals Chemotaxis-Mediated Intraorgan Crosstalk During Cardiogenesis*

The uploaded data of the authors does not contain mitochondrial reads. Therefore, we pulled and mapped the FastQ data from the four heart samples from ENA (PRJNA429249) using the FASTerQ approach with Kallisto|Bustools. Read 1 was used as the cdna read (base pairs 45 to 140, to avoid potential adaptor and poly A tails), while Read 2 was used for barcode (first 8 bp) and UMI (second 8 bp). Because of the short UMI length, we found that Kallisto|Bustools discarded many UMIs during counting. We thus used a custom script to count UMIs from the Kallisto|Bustools output.

*Michail Yekelchik et al. (Thomas Braun)*

*Mono- and multi-nucleated ventricular cardiomyocytes constitute a transcriptionally homogenous cell population*

We pulled the mapped BAM files of wild-type cells from ENA (PRJEB29049) and recounted using FeatureCounts. However, we found that the dataset had high mitochondrial read percentage, and thus we discarded this dataset.

#### **Human In Vivo.**

*Michaela Asp and Stefania Giacomello et al. (Joakim Lundberg)*

*A Spatiotemporal Organ-Wide Gene Expression and Cell Atlas of the Developing Human Heart*

We pulled the UMI data and annotations for the single cell sequencing data from the authors' website (<https://www.spatialresearch.org/resources-published-datasets/doi-10-1016-j-cell-2019-11-025/>). We used the authors' clustering and selected all cells classified as cardiomyocytes.

*Yueli Cui, Yuxuan Zheng, and Xixi Liu et al. (Jie Qiao, Fuchou Tang)*

*Single-Cell Transcriptome Analysis Maps the Developmental Track of the Human Heart*

The uploaded data of the authors does not contain mitochondrial reads. Therefore, we pulled and mapped the FastQ data from the four heart samples from ENA (PRJNA415637) using the FASTERQ approach with Kallisto|Bustools. Read 1 was used as the cDNA read (base pairs 45 to 140, to avoid potential adaptor and poly A tails), while Read 2 was used for barcode (first 8 bp) and UMI (second 8 bp). We then performed UMAP + clustering in Seurat, and selected clusters that clearly expressed cardiomyocyte markers. Because of the short UMI length, we found that Kallisto|Bustools discarded many UMIs during counting. We thus used a custom script to count UMIs from the Kallisto|Bustools output. We subsequently found that some, though not all, samples had unusually high mitochondrial percentages (namely - HE13W RV; HE17W AV, LA, LV, TV; HE20W RA; HE25W all samples). We also removed samples as post-filtering, there were too few for useful analysis (namely - HE23W, HE24W).

*Makoto Sahara and Federica Santoro et al. (Kenneth Chien)*

*Population and Single-Cell Analysis of Human Cardiogenesis Reveals Unique LGR5 Ventricular Progenitors in Embryonic Outflow Tract*

We downloaded the raw FastQ data from ENA (PRJNA510181), and subsequently mapped using Kallisto (pseudo in batch mode with the -quant flag). We had some concerns about several timepoints in this study due to high mitochondrial percentage. We eliminated some (namely - HE7W OFT, A; and HE8W); however, we are somewhat unsure about the quality of the data HE7W onwards.

*Hemant Suryawanshi et al. (Jill Buyon, Thomas Tuschl)*

*Cell atlas of the foetal human heart and implications for autoimmune-mediated congenital heart block*

The UMI data for the wild-type hearts was kindly provided by the authors as a Seurat object, and also included the authors' UMAP clustering. We utilized their clustering to identify and select cardiomyocytes; we additionally filtered out cells with notably high mitochondrial percentage or low counts/genes.

*Li Wang, Peng Yu, Bingying Zhou, and Jiangping Song et al. (Shengshou Hu)*

*Single-cell reconstruction of the adult human heart during heart failure and recovery reveals the cellular landscape underlying cardiac function*

We download the UMI data and phenotype tables provided by the authors at GEO (GSE109816), selecting only the healthy heart tissue data. We used the authors' provided metadata to select cardiomyocytes. We found that three of the four ventricular donors had extremely high mitochondrial percentages (~70%). Very little is currently known about human adult CMs, so it is difficult to assess the validity of this range. However, one ventricular sample had a lower percentage, which also matched the atrial samples. We chose to therefore exclude the three samples with extremely high mitochondrial percentage, pending discovery of further information.

#### **Human Directed Differentiation.**

*Sherri Biendarra-Tiegs et al. (Timothy Nelson)*

*Single-Cell RNA-Sequencing and Optical Electrophysiology of Human Induced Pluripotent Stem Cell-Derived Cardiomyocytes Reveal Discordance Between Cardiac Subtype-Associated Gene Expression Patterns and Electrophysiological Phenotypes*

The counts data was kindly provided by the authors. We selected cardiomyocytes using the annotations provided in Figure 4 of the manuscript.

*Jared Churko et al. (Nathan Salomonis, Joseph Wu)*

*Defining human cardiac transcription factor hierarchies using integrated single-cell heterogeneity analysis*

We pulled the UMI data for all timepoints from the authors' Synapse (<https://www.synapse.org/#!Synapse:syn18078447/files/>), using the V2 chemistry.

Clayton Friedman, Quan Nguyen, and Samuel Lukowski et al. (Joseph Powell, Nathan Palpant)  
*Single-Cell Transcriptomic Analysis of Cardiac Differentiation from Human PSCs Reveals HOPX-Dependent Cardiomyocyte Maturation*

We pulled the UMI data for all timepoints from the authors' processed data upload at ArrayExpress (E-MTAB-6268, <https://www.ebi.ac.uk/arrayexpress/experiments/E-MTAB-6268/samples/>).

Hang Ruan and Yingnan Liao et al. (Leng Han, Li Wang)

*Single-cell reconstruction of differentiation trajectory reveals a critical role of ETS1 in human cardiac lineage commitment*

We pulled the UMI for the D9, D14, and D60 timepoints from the tables uploaded by the authors at GEO (GSE129987).

Adam Selewa et al. (Sebastian Pott, Anindita Basu)

*Systematic Comparison of High-throughput Single-Cell and Single-Nucleus Transcriptomes during Cardiomyocyte Differentiation*

We pulled the UMI data for the Drop-seq samples from the tables uploaded by the authors at GEO (GSE129096). However, as with several other Drop-seq datasets, we found that the data had unusually high entropy (and perhaps owing to low depth); thus, we discarded this dataset.

### Mouse Direct Reprogramming.

Nicole R. Stone and Casey A. Gifford et al. (Deepak Srivastava)

*Context-Specific Transcription Factor Functions Regulate Epigenomic and Transcriptional Dynamics during Cardiac Reprogramming*

We pulled the UMI data for the 3' study from tables uploaded by the authors at GEO (GSE131328). We subsequently performed TSNE + clustering through Seurat and compared the generated clusters to those in the manuscript to assign cells into the putative trajectory reprogramming groups (as done by the authors).

### References

1. O Martinez, MH Reyes-valdes, Defining diversity, specialization, and gene specificity in transcriptomes through information theory. *Proc. Natl. Acad. Sci.* **105**, 9709–9714 (2008).
2. BD Macarthur, IR Lemischka, Statistical Mechanics of Pluripotency. *Cell* **154**, 484–489 (2013).
3. B Vieth, S Parekh, C Ziegenhain, W Enard, I Hellmann, A systematic evaluation of single cell RNA-seq analysis pipelines. *Nat. Commun.* **10**, 1–11 (2019).
4. AN Malik, A Czajka, P Cunningham, Accurate quantification of mouse mitochondrial DNA without co-amplification of nuclear mitochondrial insertion sequences. *Mitochondrion* **29**, 59–64 (2016).
5. S Kannan, et al., Large particle fluorescence-activated cell sorting enables high-quality single-cell RNA sequencing and functional analysis of adult cardiomyocytes. *Circ. Res.* (2019).
6. S Parekh, et al. *Gigascience* (year?).
7. P Melsted, et al., Modular and efficient pre-processing of single-cell RNA-seq. *bioRxiv*, 1–18 (2019).
8. T Ilicic, et al., Classification of low quality cells from single-cell RNA-seq data. *Genome Biol.* **17**, 1–15 (2016).
9. MD Luecken, FJ Theis, Current best practices in single-cell RNA-seq analysis : a tutorial. *Mol. Syst. Biol.* **15** (2019).
10. DJ McCarthy, KR Campbell, ATL Lun, QF Wills, Scater: pre-processing, quality control, normalization and visualization of single-cell RNA-seq data in R. *Bioinformatics* **33**, 1179–1186 (2017).
11. D Osorio, J Cai, Systematic determination of the mitochondrial proportion in human and mice tissues for single-cell RNA sequencing data quality control. *bioRxiv* (2020).
12. Y Tan, P Cahan, SingleCellNet: a computational tool to classify single cell RNA-Seq data across platforms and across species. *bioRxiv* (2018).
13. T Abdelaal, et al., A comparison of automatic cell identification methods for single-cell RNA sequencing data. *Genome Biol.* **20**, 1–19 (2019).
14. TM Consortium, Single-cell transcriptomics of 20 mouse organs creates a Tabula Muris. *Nature* **562** (2018).
15. C Ziegenhain, et al., Comparative Analysis of Single-Cell RNA Sequencing Methods. *Mol. Cell*, 631–643 (2017).
16. A Haque, J Engel, SA Teichmann, T Lönnberg, A practical guide to single-cell RNA- sequencing for biomedical research and clinical applications. *Genome Medicine* **9**, 1–12 (2017).
17. MJ Zhang, V Ntranos, D Tse, Determining sequencing depth in a single-cell RNA-seq experiment. *Nat. Commun.* **11**, 1–11 (2020).
18. JW Bagnoli, et al., Sensitive and powerful single-cell RNA sequencing using mcSCRb-seq. *Nat. Commun.* **9** (2018).

Supplementary Table 1: In Vivo Datasets										
	Isolation	Sequencing	Mapping	Datatype	Depth	Genes	Cells	Timepoints	DOI	Species
Asp and Giacomello	10x Chromium V2	10x Chromium	CellRanger	UMIs	11501.5	2899.0	762	HE7W	doi:10.1016/j.cell.2019.11.025	human
10x Chromium Demo	10x Chromium V3	10x Chromium	CellRanger	UMIs	29833.0	4872.0	178	e18	10x website	mouse
Cui, Zheng, and Liu	Picked	8bp-STRT-seq	Kallisto/Bustools	UMIs	33988.5	3834.5	2224	HE9W, HE7W, HE6W, HE5W, HE25W, HE24W, HE23W, HE22W, HE20W, HE17W, HE15W, HE13W, HE10W	doi:10.1016/j.celrep.2019.01.079	human
DeLaughter and Bick	Fluidigm C1	Smart-seq2	STAR/FeatureCounts	Reads	950178.7	5751.0	630	p0, e18, e14, e9, p3, e11, p21, p7	doi:10.1016/j.devcel.2016.10.001	mouse
De Soysa	10x Chromium V2	10x Chromium	CellRanger	UMIs	17636.5	4331.0	6836	e7.75, e8.25, e9.25	doi:10.1038/s41586-019-1414-x	mouse
Dong	Picked	8bp-STRT-seq	Kallisto/Bustools	UMIs	12444.0	2079.0	381	e9.5, e10.5, e11.5	doi:10.1186/s13059-018-1416-2	mouse
Duan 10x	10x Chromium V2	10x Chromium	CellRanger	UMIs	6705.0	2137.0	2287	p0	doi:10.1016/j.celrep.2019.05.079	mouse
Duan Drop-seq	Drop-seq	Drop-seq	Drop-seq Tools	UMIs	4100.0	1700.0	5147	p0	doi:10.1016/j.celrep.2019.05.079	mouse
Dueck	FACS	TruSeq	Kallisto	Reads	25385903.8	13382.0	18	e14.5	doi:10.1186/s13059-015-0683-4	mouse
Gladka and Molenaar	FACS	CEL-seq	BWA-ALN	UMIs	23175.0	266.0	987	p56	doi:10.1161/CIRCULATIONAHA.117.030742	mouse
Goodyer AVN	10x Chromium V2	10x Chromium	CellRanger	UMIs	10691.5	2710.0	2844	e16.5	doi:10.1161/CIRCRESAHA.118.314578	mouse
Goodyer PF	10x Chromium V2	10x Chromium	CellRanger	UMIs	8832.0	2386.0	7177	e16.5	doi:10.1161/CIRCRESAHA.118.314578	mouse
Hill e10.5	10x Chromium V2	10x Chromium	CellRanger	UMIs	19166.0	4204.0	8375	e10.5	doi:10.1242/dev.180398	mouse
Hill e13.5	10x Chromium V2	10x Chromium	CellRanger	UMIs	6677.0	2270.0	13169	e13.5	doi:10.1242/dev.180398	mouse
Jia, Preussner, and Chen	Fluidigm C1	Smart-seq2	STAR	Reads	2831162.6	7033.0	421	e8.5, e7.5, e9.5	doi:10.1038/s41467-018-07307-6	mouse
Kannan Chamber	LP-FACS	SCRB-seq	zUMIs	UMIs	51454.0	4181.5	316	p84	doi:10.1161/CIRCRESAHA.119.315493	mouse
Kannan Chamber 3' Counts	LP-FACS	SCRB-seq	zUMIs	3' Counts	361421.0	4181.5	316	p84	doi:10.1161/CIRCRESAHA.119.315493	mouse
Kannan Fixed	LP-FACS	SCRB-seq	zUMIs	UMIs	47500.5	4094.5	72	p84	doi:10.1161/CIRCRESAHA.119.315493	mouse
Kannan Fixed 3' Counts	LP-FACS	SCRB-seq	zUMIs	3' Counts	847261.0	4094.5	72	p84	doi:10.1161/CIRCRESAHA.119.315493	mouse
Kannan Reference	LP-FACS	mcSCRB-seq	zUMIs	UMIs	14801.0	3000.0	936	e18, e14, p0, p4, p14, p22, p28, p35, p56, p18, p11, p8	current manuscript	mouse
Kannan Reference 3' Counts	LP-FACS	mcSCRB-seq	zUMIs	3' Counts	39128.0	3000.0	936	e18, e14, p0, p4, p14, p22, p28, p35, p56, p18, p11, p8	current manuscript	mouse
Lescroart, Wang, and Lin	FACS	Smart-seq2	GSNAP/HTSeq	Reads	1281114.0	10257.0	807	e7.25, e6.75, e7.5, e6.5	doi:10.1126/science.aao4174	mouse
Li and Xu	Fluidigm C1	Smart-seq2	STAR/HTSeq	Reads	1754692.0	7838.0	1829	e9.5, e10.5, e8.5	doi:10.1016/j.devcel.2016.10.014	mouse
Li 10x	10x Chromium V2	10x Chromium	CellRanger	UMIs	9225.5	2685.0	4536	e10.5	doi:10.1242/dev.173476	mouse
Murphy	LP-FACS	SCRB-seq	zUMIs	UMIs	47668.0	7044.0	653	p0, p7, p28, p21, p14	doi:10.1101/2020.02.06.937797	mouse
Murphy 3' Counts	LP-FACS	SCRB-seq	zUMIs	3' Counts	279638.0	7044.0	653	p0, p7, p28, p21, p14	doi:10.1101/2020.02.06.937797	mouse
Nomura and Satoh	Picked	Smart-seq2	STAR/FeatureCounts	Reads	1670256.0	6292.0	89	p56	doi:10.1038/s41467-018-06639-7	mouse
Pijuan-Sala, Griffiths, and Guibentif	10x Chromium V1	10x Chromium	CellRanger	UMIs	14718.0	3466.5	1206	e7.75, e8.0, e8.5, e8.25	doi:10.1038/s41586-019-0933-9	mouse
Sahara and Santoro	Picked	Smart-seq2	Kallisto	Reads	1252637.4	15625.0	675	HE6.5W, HE7W, HE8W, HE7.5W, HE5W, HE8.5W, HE5.5W	doi:10.1016/j.devcel.2019.01.005	human
Sereti, Nguyen, and Kamran	Fluidigm C1	Smart-seq2	Kallisto	Reads	387744.7	5714.0	123	e9.5, e12.5, p1	doi:10.1038/s41467-018-02891-z	mouse
Suryawanshi	10x Chromium V2	10x Chromium	Drop-seq Tools	UMIs	2854.0	998.0	4918	HE19W, HE22W	doi:10.1093/cvr/cvz257	human
Tabula Muris Senis	Picked	Smart-seq2	STAR/FeatureCounts	Reads	2306773.4	2375.0	441	p720, p84	doi:10.1101/661728	mouse
Wang, Yu, Zhou, and Song	iCell8	Unknown	STAR/FeatureCounts	UMIs	55018.0	2634.0	5229	HP21Y, HP42Y, HP46Y, HP48Y, HP45Y, HP52Y, HP51Y, HP33Y, HP43Y, HP36Y	doi:10.1038/s41556-019-0446-7	human
Wunnemann and Ta-Shma	Drop-seq	Drop-seq	Drop-seq Tools	UMIs	3390.0	1460.0	26111	e14.5, e16.5, e18.5, p1, p4, p7	doi:10.1038/s41588-019-0536-2	mouse
Xiao	Drop-seq	Drop-seq	Drop-seq Tools	UMIs	1567.0	1018.0	3673	e13.5, e14.5	doi:10.1016/j.devcel.2018.03.019	mouse
Xiong, Luo, Yue, and Zhang	Picked	8bp-STRT-seq	Kallisto/Bustools	UMIs	23780.5	4556.0	1056	e9.25, e8.25, e8.75	doi:10.1161/CIRCRESAHA.119.315243	mouse
Yekelchyk	iCell8	SMARTer 3'	STAR/FeatureCounts	3' Counts	310298.7	4425.0	709	p168	doi:10.1007/s00395-019-0744-z	mouse

Supplementary Table 2: PSC-CM and iCM Datasets

	<b>Isolation</b>	<b>Sequencing</b>	<b>Mapping</b>	<b>Datatype</b>	<b>Depth</b>	<b>Genes</b>	<b>Cells</b>	<b>Timepoints</b>	<b>DOI</b>	<b>Species</b>
Biendarra-Tiegs	Fluidigm C1	Smart-seq2	MAP-Rseq	Reads	3823726.0	9912	45	D12, D40	doi:10.1089/scd.2019.0030	human
Churko	10x Chromium V2	10x Chromium	CellRanger	UMIs	11868.5	2758	13594	D0, D5, D14, D45	doi:10.1038/s41467-018-07333-4	human
Friedman, Nguyen, and Lukowski	10x Chromium V1	10x Chromium	CellRanger	UMIs	8930.0	2416	44019	D0, D2, D5, D15, D30	doi:10.1016/j.stem.2018.09.009	human
Ruan and Liao	iCell8	Unknown	STAR/FeatureCounts	UMIs	18607.5	2019	3600	D9, D14, D60	doi:10.1186/s12915-019-0709-6	human
Selewa	Drop-seq	Drop-seq	STAR/FeatureCounts	UMIs	1613.0	1057	37302	D0, D1, D3, D7, D15	doi:10.1038/s41598-020-58327-6	human
Stone and Gifford	10x Chromium V2	10x Chromium	CellRanger	UMIs	11302.0	3111	30728	DM1, D1, D2, D3, D7, D14	doi:10.1016/j.stem.2019.06.012	mouse